NOVA SCHOOL OF SCIENCE & TECHNOLOGY

DEPARTMENT OF CHEMISTRY

DANIELA LEONARDO DUARTE

BSc in Applied Chemistry

MODIFYING THE SURFACE OF MESOPOROUS SILICA FOR TUNING THE DRUG RELEASE PROFILE

MASTER IN BIOORGANIC CHEMISTRY

NOVA University Lisbon
September, 2023

NOVA SCHOOL OF SCIENCE & TECHNOLOGY

DEPARTMENT OF CHEMISTRY

MODIFYING THE SURFACE OF MESOPOROUS SILICA FOR TUNING THE DRUG RELEASE PROFILE

DANIELA LEONARDO DUARTE

BSc in Applied Chemistry

Adviser: Inês Matos
Principal Investigator, FCT-UNL

Co-adviser: María Teresa Viciosa Plaza
Auxiliary Investigator, IST/UL

Examination Committee

Chair: Prof. Doutora Luísa Ferreira
FCT-UNL

Member: Prof. Doutora Madalena Dionísio
FCT-UNL

MASTER IN BIOORGANIC CHEMISTRY

NOVA University Lisbon
September, 2023

Modifying the surface of mesoporous silica for tuning the drug release profile

This document was created with the (pdf/Xe/Lua)LaTeX processor and the NOVAthesis template (v6.9.5) [1].

Acknowledgements

First and foremost, i would like to thank my advisors. To Professor María Teresa Viciosa Plaza for aceepting to guide me on this journey. All of the hours spent helping me understand my work and introducing new techniques won't be forgotten. Not only that, but i also got the opportunity to work in another university and experience a new environment and for that i am grateful. To Professor Inês Matos for giving me the tools to grow in the laboratory and always sparing a moment to provide advice and enable improvement on my part.

To Professor João Sotomayor for the assistance with the samples prepared in vacuum.

To everyone in laboratory 122 who contributed to the pleasant environment, in specific to Andreia Santos for the frequent moments of support and for taking the time to help with my samples, even with her busy schedule.

To Pedro Rosa for teaching me how to prepare TEM and NMR samples and acquiring the TEM images. To Inês Santos for aqcuiring the NMR spectra and always providing company.

To Patrícia Rodrigues for supporting me the whole journey, even with no knowledge of chemistry, and for being my tech support. To Bagheera, the bunny with the biggest personality, for her soothing presence and emotional support.

Last but not least, to all my family and friends who stood by me and contributed one way or another to make this experience possible.

"I am among those who think that science has great beauty." (Marie Curie)

Abstract

This thesis aims to contribute to the problem of low solubility drugs, using efavirenz as a model compound. For this aim, the strategy was incorporating efavirenz on a mesoporous silica MCM-41 matrix, to stabilize the amorphous state and improve solubility. Additionally, the functionalized silicas were also synthesized in an effort to tune the release of the drug. The sucess of synthesis of MCM-41 and modified silica by one pot method was confirmed by nitrogen porosimetry analysis, elemental analysis, transmission electron spectroscopy (TEM), infrared spectroscopy (ATR-FTIR) and nuclear magnetic resonance (NMR).

The drug loading was performed from a high concentration solution in ethanol, to achieve a 30% pore filling degree. The native efavirenz and resulting composites (EFZ:MCM-41, EFZ:NH_2-MCM-41, EFZ:CH_3-MCM-41 and EFZ:SH-MCM-41) were analyzed by ATR-FTIR, differential scanning calorimetry (DSC) and dielectric relaxation spectroscopy (DRS). The stabilization of the amorphous state was corroborated by the presence of the glass transition step by DSC analysis. Remnants of crystalline efavirenz were detected in two composites (EFZ:NH_2-MCM-41 and EFZ:CH_3-MCM-41) by the presence of the melting peak (T_m=137 °C). The molecular mobility of efavirenz was probed by DRS. For EFZ:NH_2-MCM-41 the dielectric spectra was analyzed in detail, allowing the estimation of a dielectric glass transition temperature in accordance with the calorimetric one.

The release profiles of the composites were performed in a phosphate buffer solution, pH=7.4, 37 °C and 100 rpm to simulate the intestinal fluid. The amount of drug released was analyzed with Uv-Vis spectroscopy. When compared to EFZ:MCM-41, EFZ:CH_3-MCM-41 and EFZ:SH-MCM-41 showed slower dissolution percentages for 48 hours, while EFZ:NH_2-MCM-41 resulted in a faster kinetics.

Keywords: Solubility, efavirenz, MCM-41, glass transition, pore functionalization

Resumo

Este trabalho pretendeu ser uma contribuição para o problema de fármacos com baixa solubilidade, utilizando como fármaco alvo o efavirenz. Assim sendo, a estratégia utilizada foi a incorporação de efavirenz em sílica mesoporosa MCM-41, para estabilizar o estado amorfo e melhorar a solubilidade. Adicionalmente, sílicas funcionalizadas foram também sintetizadas de modo a controlar a libertação do fármaco. O sucesso da síntese das matrizes através do método *one pot* foi confirmado através de adsorção de azoto, análise elementar, microscopia eletrônica de transmissão (TEM), espectroscopia de infravermelho (ATR-FTIR) e ressonânica magnética nuclear (RMN).

A impregnação do fármaco foi efetuada com uma solução concentrada em etanol, para obter preenchimento do poro de 30%. O fármaco e compósitos resultantes (EFZ:MCM-41, EFZ:NH_2-MCM-41, EFZ:CH_3-MCM-41 e EFZ:SH-MCM-41) foram analisados por ATR-FTIR, calorimetria de varrimento diferencial (DSC) e espectroscopia de relaxação dieléctrica (DRS). A estabilização do estado amorfo foi confirmada com a presença da transição vítrea por análise de DSC. A presença de efavirenz cristalino foi detetada em dois compósitos (EFZ:NH_2-MCM-41 e EFZ:CH_3-MCM-41) através do pico de fusão do fármaco (T_m=137 °C). A mobilidade molecular do efavirenz foi estudada por DRS. Para EFZ:NH_2-MCM-41 o espetro dieléctrico foi analisado em detalhe, permitindo a estimativa da temperatura de transição vítrea dieléctrica que está em boa concordância com a temperatura calorimétrica.

Os ensaios de libertação dos compósitos foram relizados em solução tampão fosfato, pH=7.4, 37 °C e 100 rpm para simular o fluído intestinal. A quantidade de efavirenz libertada foi analisada com espectroscopia Uv-Visível. Quando comparados com EFZ:MCM-41, os compósitos EFZ:NH_2-MCM-41 e EFZ:CH_3-MCM-41 demonstraram percentagens de dissolução menores para 48 h, enquanto EFZ:NH_2-MCM-41 apresenta uma cinética mais rápida.

Palavras-chave: Solubilidade, efavirenz, MCM-41, transição vítrea

Contents

List of Figures ix

List of Tables xii

Acronyms xiii

Symbols xiv

1 Introduction 1

1.1 Biopharmaceutics Classification System (BCS) . . . 2
1.2 Structure of Solid Materials . . . 2
1.3 Glass Transition . . . 3
1.4 Efavirenz . . . 4
1.5 Mesoporous MCM-41 Silica . . . 5
1.6 MCM-41 Funcionalization . . . 6
1.7 Techniques . . . 6
1.7.1 Attenuated Total Reflectance Fourier Transform Infrared Spectroscopy (ATR-FTIR) . . . 6
1.7.2 Transmission Electron Microscopy (TEM) . . . 7
1.7.3 Differential Scanning Calorimetry (DSC) . . . 7
1.7.4 Dielectric Relaxation Spectroscopy (DRS) . . . 10
1.7.5 Nuclear Magnetic Resonance (NMR) . . . 11
1.7.6 Ultraviolet-visible Spectroscopy . . . 11
1.8 Main Goals of Thesis . . . 12
1.9 Thesis Outline . . . 12

2 Materials and Methods 13

2.1 Synthesis of MCM-41 . . . 13
2.2 Funcionalization of MCM-41 . . . 13
2.3 Nitrogen Adsorption . . . 14

2.4 Elemental Analysis . . . 14
2.5 Transmission Electron Microscopy (TEM) . . . 14
2.6 Differential Scanning Calorimetry (DSC) . . . 14
2.7 Efavirenz Loading . . . 14
2.8 Attenuated Total Reflectance Fourier Transform Infrared Spectroscopy (ATR-FTIR) . . . 15
2.9 Dielectric Relaxation Spectroscopy (DRS) . . . 15
2.10 Ultraviolet-Visible Spectroscopy . . . 15
2.11 Nuclear Magnetic Ressonance . . . 16
2.12 Controled Release Experiments . . . 16

3 Results and Discussion **17**
3.1 Nitrogen Adsorption . . . 17
3.2 Attenuated Total Reflection Fourier Transform Infrared Spectroscopy (ATR-FTIR) . . . 18
3.2.1 Efavirenz . . . 22
3.2.2 Loaded Silica . . . 23
3.3 Elemental Analysis . . . 24
3.4 Nuclear Magnetic Ressonance (NMR) . . . 25
3.5 Transmission Electron Microscopy (TEM) . . . 27
3.6 Differential Scanning Calorimetry (DSC) . . . 29
3.6.1 Determination of melting and glass forming possibility . . . 29
3.6.2 Determining the necessary conditions for cold crystallization . . . 30
3.6.3 Investigating isothermal crystallization . . . 33
3.6.4 Investigating crystallization kinetics . . . 35
3.6.5 Unloaded Silica . . . 37
3.6.6 Loaded Silica . . . 38
3.7 Dielectric Relaxation Spectroscopy (DRS) . . . 39
3.7.1 Efavirenz . . . 39
3.7.2 Unloaded and Loaded Silica . . . 43
3.8 Controled Release Studies . . . 53

4 Conclusion **57**

5 Future Works **59**

Bibliography **60**

Appendices

A Appendices **68**

List of Figures

1.1 Solubility of top 200 oral drugs in Europe and US (adapted from [5]). . . . 1
1.2 Temperature dependence of a liquid's volume (v), entropy (S) or enthalpy (H) at constant pressure (adapted from [20]). 3
1.3 Structural formula of efavirenz (S enantiomer). 4
1.4 Four main groups of the M41S family (adapted from [29]). 5
1.5 Schematic representation of an ATR crystal (adapted from [38]). 7
1.6 Heat-flux differential scanning calorimetry cells (adapted from [42]). 9
1.7 DSC thermogram of undried sucrose, with glass transition temperature (T_g), recrystallization endotherm temperature (T_c) and enthalpy (ΔH_c), melting endotherm temperature (T_m) and enthalpy (ΔH_f). Endothermic transitions are down (adapted from [42]). 10

3.1 Nitrogen adsorption-desorption isotherms of MCM-41, NH_2-MCM-41, CH_3-MCM-41 and SH-MCM-41. 17
3.2 ATR-FTIR spectra of the unmodified silica. 19
3.3 ATR-FTIR spectra of the MCM-41 (black) and NH_2-MCM-41 (blue) silica. . 20
3.4 ATR-FTIR spectra of the MCM-41 (black) and CH_3-MCM-41 (green) silica. 21
3.5 ATR-FTIR spectra of the MCM-41 (black) and SH-MCM-41 (red) silica. . . 22
3.6 ATR-FTIR spectra of efavirenz. 23
3.7 ATR-FTIR spectra of bulk efavirenz (dotted black), EFZ:MCM-41 (black), EFZ:NH_2-MCM-41 (blue), EFZ:CH_3-MCM-41 (green) and EFZ:SH-MCM-41 (red) samples. All curves were vertically displaced for a better visualization. 24
3.8 ^{1}H NMR spectra for NH_2-MCM-41 in NaOH/D_2O. The internal standard peak is at 5.09 ppm. CTAB peak is marked with (*). 26
3.9 ^{1}H NMR spectra for CH_3-MCM-41 in NaOH/D_2O. The internal standard peak is at 5.07 ppm. CTAB peaks are marked with (*). 26
3.10 ^{1}H NMR spectra for SH-MCM-41 in NaOH/D_2O. The internal standard peak is at 5.07 ppm. CTAB peak is marked with (*). 27
3.11 TEM images of MCM-41 (a, b), NH_2-MCM-41 (c, d), CH_3-MCM-41(e, f) and SH-MCM-41 (g, h). 28

3.12 DSC thermograms of bulk efavirenz at 10 °C/min: (i) during heating, from 25 °C to 155 °C(orange);(ii) during cooling, from 155 °C to -80 °C(light blue); (iii) during heating, from -80 °C to 155 °C(purple). The glass transition region on heating was enlarged in the inset (mass = 2.86 mg). 30
3.13 C(a) Experimental procedure followed; (b) DSC thermogram of bulk efavirenz during heating at 5 °C/min after previous cooling at 10 °C/min down to different temperatures (T=40, 20, 0, -20, -40, -60 °C). The glass transition region was enlarged (mass=3.81mg). 31
3.14 DSC thermograms of bulk efavirenz at 10 °C/min: (i) during cooling, from 155 °C to -40 °C (blue); (ii) during heating, from -40 °C to 155 °C (green). . 32
3.15 (a) Experimental procedure followed; (b) Thermogram obtained during the isothermal at 85 °C (ΔH_m=36.83 J/g); (c) Thermogram obtained on heating at 10 °C/min after isothermal crystallization at 85 °C (mass=3.81 mg). 34
3.16 (a) Experimental procedure followed; (b) Thermogram obtained during the isothermals at 74 °C, 80 °C, 84 °C, 88 °C and 100 °C. All the isothermals were corrected to start at t=0 minutes. Only the first 30 minutes of the isothermals are represented for better visualization of the crystallization signal (mass=3.79 mg). 35
3.17 (a) Heating thermograms obtained at 10 °C/min after different isothermal crystallizations shown in figure 3.16 (mass=3.79 mg). 36
3.18 DSC thermograms of MCM-41 (a), NH_2-MCM-41 (b), CH_3-MCM-41 (c) and SH-MCM-41 (d) at 10 °C/min: (i) during heating, from -50 °C to 140 °C (green); (ii) during cooling, from 140 °C to -50 °C (red); during heating, from -50 °C to 140 °C (purple). 37
3.19 DSC thermogram of: a) EFZ:MCM-41 at 10 °C/min^{-1} (mass=4.33mg); b) EFZ:NH_2-MCM-41 at 10 °C/min^{-1} (mass=4.28mg); c) EFZ:CH_3-MCM-41 at 10 °C/min^{-1} (mass=4.41mg); d) EFZ:SH-MCM-41 at 10 °C/min^{-1} (mass=3.80mg). 38
3.20 a)Isochronal representation of ε' at the frequency of 10^4 Hz: the black symbols (square) correspond to the cooling of the sample at 10 °C/min and red symbols (circle) correspond to the subsequent cooling at 10 °C/min; b)Thermogram of bulk efavirenz during cooling at 10 °C/min, from 155 °C to -40 °C (from figure 3.14). 40
3.21 Permittivity spectra of efavirenz taken at 80 °C. The spectra were collected every 90 s for the first 3510 s, and every 180 s for another 4680 s. 41
3.22 Dielectric spectrum collected for crystallization (80 °C) at: a) 180 s; b) 8010 s. Individual fitting functions are represented by colored lines, the overall fitting by a black line and experimental data by open circles. 42
3.23 Time evolution of: a) dielectric strength, $\delta\varepsilon_\alpha(t)$, for the amorphous fraction; b) crystallinity degree estimated following equation 3.11. Cold crystallization monitored at 80 °C and followed during 8010 s. Solid line represents the fit with equation 3.10 43

3.24 Isochronal representation of ε' (left) and ε" (right), at the frequency 1 kHz for unloaded silica: (a, b) MCM-41; (c, d) NH_2-MCM-41; (e, f) CH_3-MCM-41 and (g, h) SH-MCM-41. Blue and red data correspond to first and second heating respectively. 44
3.25 Isothermal M" and ε" spectra of unloaded NH_2-MCM-41 matrix for temperatures from -110 to 50 °C every 5 degrees. 45
3.26 Dielectric spectrum taken at 95 °C for: a) the first serie and b) the second serie of NH_2-MCM-41. The colored lines represent the fitting of data. 46
3.27 Relaxation map of all processes detected in unloaded matrices NH_2-MCM-41, $MCM\text{-}41_2$ [69] and MSN_APTES [70] (fitting in M"(f)). 47
3.28 Isothermal representation of ε' (left) and ε" (right) vs. temperature at f=1 kHz for (a,b) efavirenz, (c,d) EFZ:MCM-41, (e,f) EFZ:NH_2-MCM-41, (g,h) EFZ:CH_3-MCM-41 and (i,j) EFZ:SH-MCM-41. The filled and open symbols are for hydrated and dried data, respectively. 49
3.29 Dielectric spectrum taken at 60 °C for: a) bulk efavirenz and b) the first series of EFZ:NH_2-MCM-41. The colored lines represent the fitting of data. . . . 50
3.30 Relaxation map of all processes detected in EFZ:NH_2-MCM-41 (blue symbols) and bulk efavirenz (red symbols). Filled and open symbols correspond to hydrated and dried data, respectively. The solid lines are fitting functions with VFTH estimated for each process. 51
3.31 In vitro release profiles of native efavirenz and: a) EFZ:MCM-41; b)EFZ:NH_2-MCM-41; c) EFZ:CH_3-MCM-41 and d) EFZ:SH-MCM-41. 53
3.32 In vitro release profiles of native efavirenz and: a) EFZ:MCM-41; b)EFZ:NH_2-MCM-41; c) EFZ:CH_3-MCM-41 and d) EFZ:SH-MCM-41. Zoom on the first 100 minutes. 54
3.33 In vitro release profiles of EFZ:MCM-41 (purple), EFZ:NH_2-MCM-41 (blue) and EFZ:CH_3-MCM-41 (green). 55

A.1 Thermogram obtained on heating at 10 °C/min after isothermal crystallization at 85 °C, for the 0-70 °C. 68
A.2 Isothermal M" spectra of: a) NH_2-MCM-41, b)CH_3-MCM-41 and c)SH-MCM-41 for temperatures from -100 to 10 °C every 10 degrees. 69

List of Tables

1.1 Biopharmaceutics Classification System (adapted from [10]) 2

2.1 Organosilanes used in MCM-41 functionalization 14
2.2 Masses of unloaded silica and efavirenz in order to have a pore filling of 30%. 15

3.1 Textural properties of unloaded silica. 18
3.2 Mass percentages of nitrogen, carbon, hydrogen and sulfur in all four synthesized silica. 24
3.3 Average values of length and height for syntheses mesoporous silica. 29
3.4 Values calculated from DSC thermogram displayed in figure 3.13 relative to glass transition, crystallization and melting. 32
3.5 Values calculated from the previous DSC thermogram (figure 3.16) relative to glass transition, crystallization and melting. 36
3.6 Percentage of water loss estimated by calorimeter drying. 37
3.7 Glass transition temperature at onset, midpoint and endpoint, and percentage of water loss for all four composites. 39
3.8 Activation parameters for unloaded silicas. The relaxation times of process I and II were fitted with equation 3.8. 48
3.9 Estimated parameters of VFTH fit for the α-process in all samples. 52

Acronyms

API Active Pharmaceutical Ingredients 3
APTES 3-Aminopropyl)triethoxysilane 13
ATR-FTIR Attenuated Total Reflectance Fourier Transform Infrared Spectroscopy 6

BCS Biopharmaceutics Classification System 2
BET Brunauer–Emmett–Teller 17
BJH Barrett-Joyner-Halenda 17

CTAB Cetyltrimethylammonium Bromide 5

DFT Density Functional Theory 17
DRS Dielectric Relaxation Spectroscopy 10

EFZ Efavirenz 4

HIV-1 Human Immunodeficiency Virus Type 1 4
HN Havriliak-Negami 41

MPTMS 3-Mercaptopropyl)trimethoxysilane 13
MTM Methyltrimethoxysilane 13

NMR Nuclear Magnetic Ressonance 11
NNRTI Non-Nucleoside Reverse Transcriptase Inhibitor 4

TEM Transmission Electron Microscopy 7
TEOS tetraethylorthosilicate 5

Uv-Vis Ultraviolet-Visible 11

Symbols

α_{HN} Symmetric Broadening of Complex Dielectric Function 41

β_{HN} Asymmetric Broadening of Complex Dielectric Function 41

χ_{cr} Degree of Crystallization 42

$\Delta\varepsilon$ Dielectric Strength 41
$\Delta\varepsilon_{\alpha}$ Dielectric Strength During Crystallization 42

E_a Activation Energy 51
ε^* Permittivity 10
ε' Real Part of Permittivity 10
ε'' Imaginary Part of Permittivity 10
η Viscosity 52

G Shear Modulus 52

ΔH_c Crystallization Enthalpy ix, 10
ΔH_f Melting Enthalpy ix, 10

k Rate Constant 42

m Fragility Index 52
M'' Dielectric Modulus 45
M* Complex Electrical Modulus 45

n Avrami Parameter 42

ω Angular Frequency 10

τ_{HN} HN Relaxation Time 41

T_c Crystallization Temperature ix, 10

T_g Glass Transition Temperature 3

1 Introduction

In current times, one of the most common features of pharmaceutical drugs is low water solubility. In fact, about 40% of marketed drugs as of 2006 were poorly water-soluble (see figure 1.1). One possible hypothesis for these numbers is the fact that receptor binding is partly mediated by hydrophobic interactions and drug targets that are connected to lipophilic ligands or intracellular signaling pathways [2]. This low solubility directly affects the oral adsorption since, in many situations, drug molecules need to be in solution in the gastrointestinal fluid to be adsorbed by the systemic blood stream [3]. The most direct way of getting around this issue would be using a higher concentration of the drug, although in practice this is not the safest option. Although a higher drug concentration could lead to a higher therapeutic benefit, it also carries the risk of unwanted side effects such as local toxicity [4].

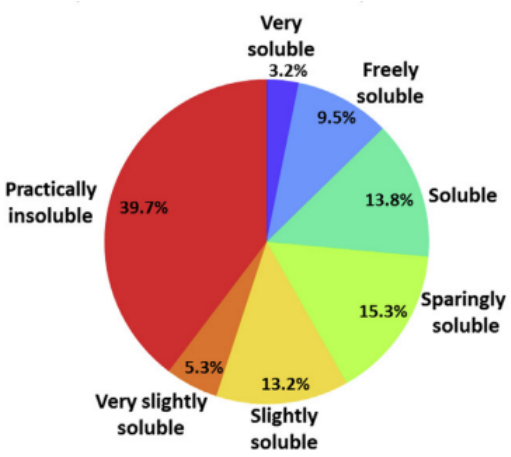

Figure 1.1: Solubility of top 200 oral drugs in Europe and US (adapted from [5]).

Currently, there are many strategies to address the low water solubility and they can be divided in three major categories: chemical, physical and administration. Chemical modifications target the pH of formulation and involve a prodrug design. Physical approaches use a modified solid state of the drug, cosolvents, among many others [6]. Finally, the administration modification simply consists of using an alternative administration route

[7] [8].

One of the physical approaches consists of modifying the solid of the drug, more specifically to obtain an amorphous solid. In this physical state, the drug-drug interactions are weaker and theoretically the solubility values can be up to 1600 higher than those of crystalline solids [5]. One example of this approach, already in use for efavirenz, refers to the use of mesoporous silica as a carrier, to combine the increased solubility of the amorphous solid and improved bioavailability and dissolution rate from the silica [9].

1.1 Biopharmaceutics Classification System (BCS)

Biopharmaceutics Classification System (BCS) is a system that classifies drugs based on their aqueous solubility and intestinal permeability in four different classes (see table 1.1) [10]. This tool allows the estimation of the contribution of solubility, dissolution and intestinal permeability, which in turn provides an opportunity for the improvement of developing drugs.

Table 1.1: Biopharmaceutics Classification System (adapted from [10])

Class	Solubility	Permeability
I	High	High
II	Low	High
III	High	Low
IV	Low	Low

Class I compounds are well absorbed and have an adsorption rate higher than excretion. Class II has a bioavailability limited by solvation rate. There is a connection between the *in vivo* bioavailability and *in vitro* solvation. For class III, although the adsorption is restricted by permeation rate and drug is solvated fast. Finally, class IV compounds have a poor bioavailability, and are badly adsorved by the intestines[11].

1.2 Structure of Solid Materials

Molecules, atoms or even ions that form solids can be arranged in an orderly or disordered manner. Crystalline solids have regularly repeated structural units, or unit cells, in the three dimensions of space. The recurrent crystalline forms of pharmaceutical compounds are polymorphs and solvates. Polymorphs have an identical chemical composition but distinct internal crystal structures, and for that reason may present different properties. This occurrence is very common among organic molecules.

Solvates are crystalline solids that contain solvent molecules in the crystalline structure. If the solvent is water, then the solvate is named hydrate [12].

On the other hand, substances in the amorphous form do not have a long rage order, though usually there is a local topological order [13]. This order will swiftly decay as distance increases in the material. Since the atomic positions are disordered, there is an

emergence of occurrences not seen in crystals, unique and important. One example of this is the distinct thermal conductivity of amorphous material which heavily impacts the electronic industry [14].

The properties and knowledge of these types of solids is particularly important in relation to Active Pharmaceutical Ingredients (API). Given the increase of poor water soluble API, there has been a need to overcome this matter. One of the most promising mechanisms is the conversion of crystalline drug compounds into their amorphous counterpart.

Considering that, when compared with its crystalline form, the amorphous form of a solid is the highest energy form, it has a greater molecular mobility and increased thermodynamic properties. These advantages are hard to maintain since these materials have a higher chemical reactivity and tendency to recrystallize at multiple stages of the drug lifetime [15]. Given this, there has been a lot of effort put into understanding the recrystallization conditions and how to better stabilize amorphous drugs [16].

1.3 Glass Transition

Glass is an amorphous material with the mechanical properties of an isotropic solid, where its physical properties are independent of the system orientation.There is still much to learn about the nature of the glassy state at the atomic level [17] .Glass can be obtained by cooling a liquid to a temperature below its glass temperature temperature, T_g. In order to avoid a first order phase transition, the quench of the material must be quick enough, leading to solidification through a gradual increase in viscosity [18] [19].

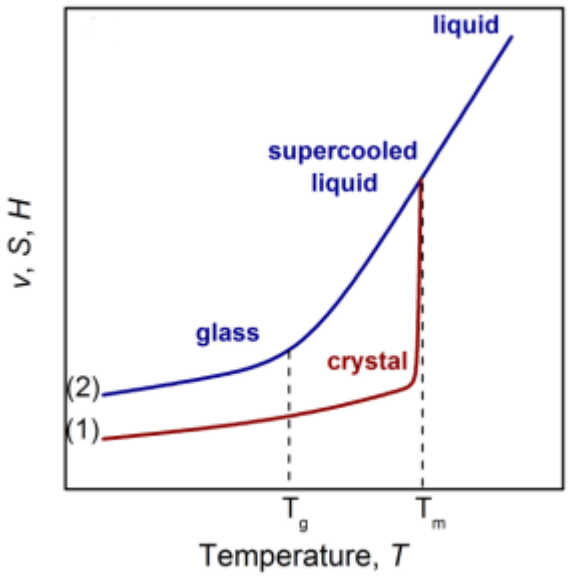

Figure 1.2: Temperature dependence of a liquid's volume (v), entropy (S) or enthalpy (H) at constant pressure (adapted from [20]).

Figure 1.2 exemplifies a liquid's volume temperature dependence at constant pressure. Molecular mobility is slowed down when a liquid is cooled below the freezing point. If the cooling is fast enough, crystallization can be avoided. The molecules will start to rearrange so slowly that they cannot position themselves in adequate configurations in the time allowed by the cooling rate. Here, the rate of change of enthaply or volume in regards to temperature decreases abruptly to a value similar to a crystalline solid, in which the resulting material is a glass. The slower the cooling, the more time there is available for configuration at each temperature and the colder it can be before losing equilibrium. As a consequence, there is an increase of glass transition temperature (T_g) with the cooling rate [21].

1.4 Efavirenz

Efavirenz (EFZ) is a Non-Nucleoside Reverse Transcriptase Inhibitor (NNRTI) of Human Immunodeficiency Virus Type 1 (HIV-1) (see figure 1.3). It is a crystalline powder, ranging from white to light pink, pratically insoluble in water with 4 polymorphs characterized in literature [22]. The S enantiomer is used for therapeutic purposes [23]. EFZ belongs to class II of the BCS system with a low water solubility of about 4 μg/mL and a limited oral bioavailability of 40-50% [8]

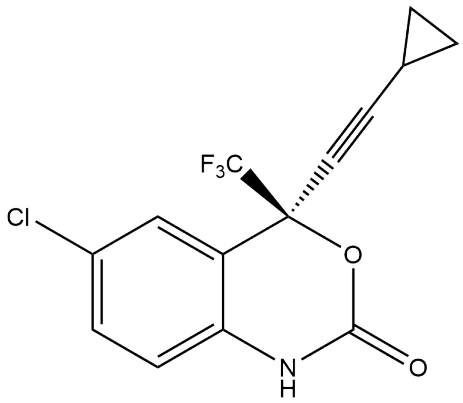

Figure 1.3: Structural formula of efavirenz (S enantiomer).

NNRTI are a class of antiretrovirals which inhibit the reverse transcriptase enzyme, a viral enzyme that transcribes viral RNA into DNA. This inhibition interferes with viral replication necessary for the spread of the disease [24]. EFZ is used for treatment along with other antiretroviral agents of different classes, as a part of highly active antiretroviral therapy (HAART). HAART decreases the patient's HIV burden, preserves function of the immune system and prevents deadly infections from occurring [25].

1.5 Mesoporous MCM-41 Silica

Mesoporous silica material were first described by Mobil Oil scientists in the 1990's [26]. This class of materials has an ordered pore distribution, with sizes between 2 and 20 nm, a large surface area and a surface densely-populated with silanol groups that can be used for future functionalizations. One of the materials that has received considerable attention is MCM-41, from the M41S family (see figure 1.4). This silica not only has the previously mentioned characteristics but also an hexagonal array of cylindrical mesopores [27] [28].

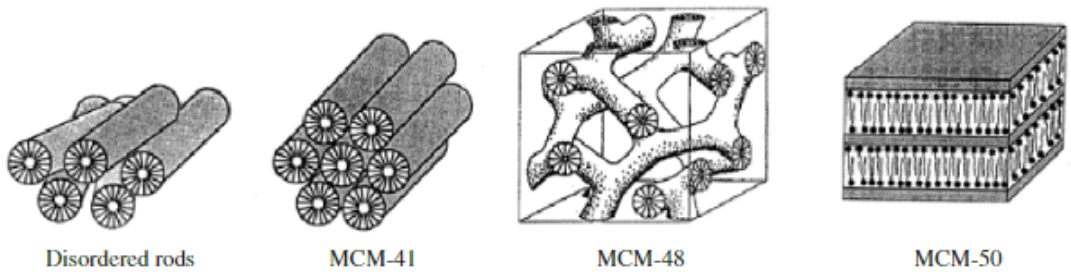

Figure 1.4: Four main groups of the M41S family (adapted from [29]).

The synthesis of this material is based on the condensation of silica precursors, such as tetraethylorthosilicate (TEOS) or sodium silicate. This condensation occurs in the presence of cationic surfactants under basic conditions. The usual preparation involves mixing TEOS with the cationic surfactant, like Cetyltrimethylammonium Bromide (CTAB), at a temperature of 30-60 °C and pH=11, in which particules will be formed by the sol-gel process.

In the first step of this process, there is hydrolysis of the alkoxide and polymerization of the silanol groups to establish a structure linked by siloxane bonds (Si-O-Si). Afterwards, the cylindrical micelles formed by the surfactant will act as a template for the pore formation. The surfactant will attract the negative charge of the silica concentrated around the micelles, therefore forming the tubular structure. These particles will continue to grow until the negative charge becomes so high that it stops the growth. Lastly, the surfactant is removed from the inside of the pores. This can be achieved in several ways: treatment with ammonium nitrate, reflux in acidified alcohol with hydrochloric acid and calcination. All of these methods rupture the electrostatic interactions between the cationic surfactant head and the anionic silicates [30].

One biomedical application of mesoporous silica that is relevant for this work is its use as a drug delivery system. It has several key features that make it an excellent candidate. These are a high surface area, with high potential for drug adsorption; high pore volume that can contain the necessary amount of drug; ordered pore network, homogenous in size and allows fine control of release kinetics; silanol surface groups that can be functionalized [31]. Additionally, silica particles appear to be biocompatible and degrade

after some time in the body [32].

1.6 MCM-41 Funcionalization

One way of diversifying the release properties of mesoporous silica materials is through surface modifications with organic and inorganic functional groups. With the use of different species, it is possible to tune the interaction of the drug with the silica, prevent particle agglomeration and even facilitate the incorporation of nanoparticles (for example gold nanoparticles) inside the pores [33] [34]. Overall, there are two methods to functionalize these materials: co-condensation and postsynthesis grafting. In the first method, the organosilane with the intended functional group is added to the synthesis, therefore the functionalized material is obtained after one step. In postsynthesis grafting, the silanol groups present in calcinated mesoporous silica react with an organoalkoxysilane reagent carrying the functional group. Both of these methods have pros and cons.

For co-condensation, there is a more even distribution of functional groups throughout the pore surface but on the other hand, extraction of surfactant can be bothersome. With postsynthesis grafting, there is more flexibility with the location of the modification. A downside of this method can be the reduction in molecule diffusion in and out of the silica by reaction of the organosilane at the mesopore opening [34] [35].

1.7 Techniques

1.7.1 Attenuated Total Reflectance Fourier Transform Infrared Spectroscopy (ATR-FTIR)

Attenuated Total Reflectance Fourier Transform Infrared Spectroscopy (ATR-FTIR) allows the investigation of molecular vibrations. A spectrometer sends infrared radiation to a sample, in which some will be passes through and the absorbed radiation is then converted into vibrational energy by the molecules. Nonlinear molecules with N atoms have 3N-6 fundamental vibrations, where linear molecules only have 3N-5 vibrations. Keeping this is mind, it is possible to associate functional groups with characteristic infrared spectroscopy bands [36].

Even before acquiring a spectrum, care with the sample preparation is required. Liquid samples are placed in between two KBr plates and solid samples have to be dissolved in an appropriate solvent, combined with nujol to form a mull or turned into a pellet. When using an ATR-FTIR equipment, the sample can be directly placed onto the prism, without any prior change. Gas samples require different equipment and greater care. After the sample has been placed in the spectrometer, it is subjected to infrared radiation. The emitted radiation is dispersed and directed to a detector, which generates a response. Subsequently, the response signal is amplified, converted into a digital signal

and transferred to a computer where it is subjected to a Fourier transform to generate an interpretable spectrum [37].

Attenuated total reflectance is used in conjuction with infrared spectroscopy to enable easier sampling and better reproducibility. Here, the infrared beam is passed through a diamond, zinc selenide or germanium crystal at an angle greater than the critical angle, leading to a total internal reflection of the beam at the crystal surface. The reflectance produce an attenuated evanescent wave. After being reflected one or more times in the crystal, the beam leaves and is recorded by the detector [38].

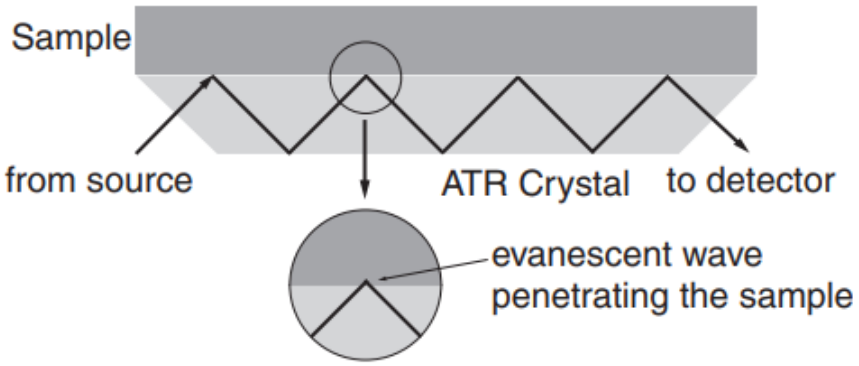

Figure 1.5: Schematic representation of an ATR crystal (adapted from [38]).

1.7.2 Transmission Electron Microscopy (TEM)

Given the increasing nature of materials with features in the nanoscopic scale, there was need for a technique more powerful than light microscopy. This is where Transmission Electron Microscopy (TEM) comes in. It uses the de Broglie wavelenght of electrons to obtain images at a considerably higher resolution. At the highest resolution, even the atomic arrangement of a crystalline system can be ascertained [39].

In this technique, an electron beam is incident onto an area of the sample. The electrons that are transmitted through the sample are then focused by lenses and collected by a parallel detector, forming an image. With this image, there are plenty of microstructural features that can be observed in materials [40].

1.7.3 Differential Scanning Calorimetry (DSC)

Differential scanning calorimetry (DSC) is a calorimetric method that allows the study of thermal transitions and reactions. This is particularly helpful when following structure alterations in a material even when there is no apparent visual change.

In the instrument, two pans are isolated from the surrounding environment in a chamber. One pan is the reference, which remains empty and the other contains the sample. Under these pans are heaters used to change the temperature and sensors to point out the temperature at any given time. These heaters heat the pans at the same rate

of temperature change, while the rate at which thermal energy is supplied to the pans, heat flow, differs. These values and difference in heat flow between the reference and samples pans is then passed on to the computer [41].

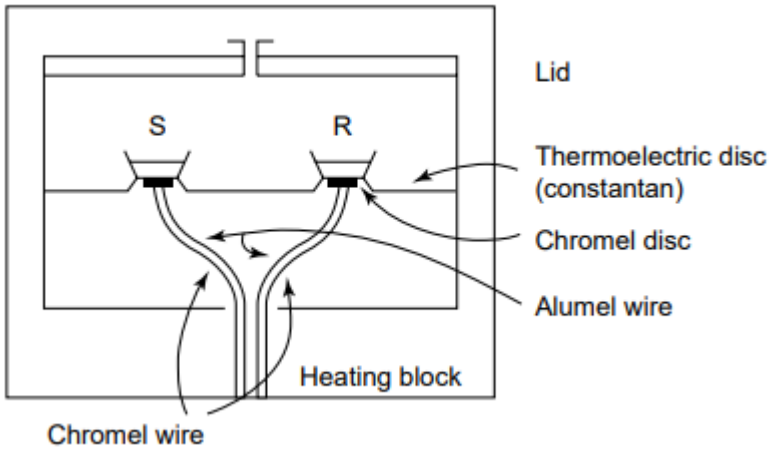

Figure 1.6: Heat-flux differential scanning calorimetry cells (adapted from [42]).

Characterized components can exhibit an array of thermal behaviors, such as melting, glass transitions or crystallization, which appear in thermograms as endothermic or exothermic peaks (see 1.7). In these experiments it is important to define the onset, extrapolated onset and offset temperatures and scanning rate used. Going further still, physical properties of the sample can also be extracted. DSC can provide accurate melting temperatures and even account for transitions between different polymorphs. The shape, width and peak height of the melting endotherm will also provide information about the sample. Crystallinity can not only be detected but also quantified. Detecting the conversion between the amorphous and crystalline form is critical when dealing with pharmaceutical compounds, since this will impact the physico-chemical stability of the dosage form [42].

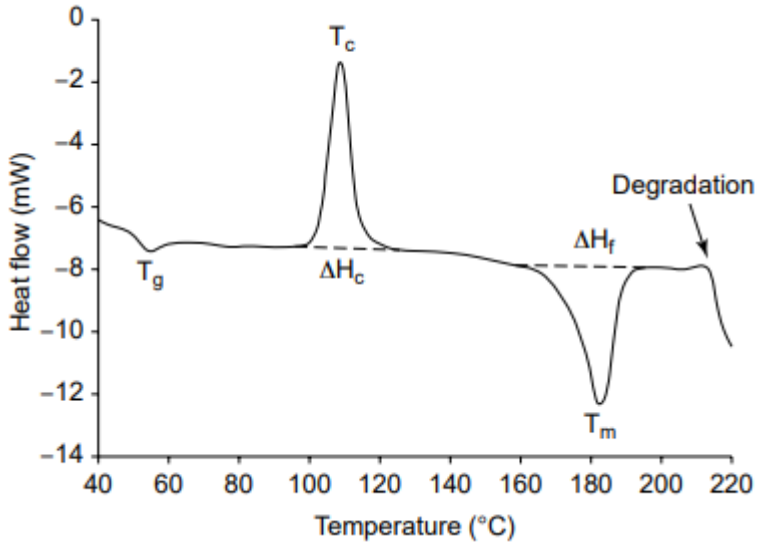

Figure 1.7: DSC thermogram of undried sucrose, with glass transition temperature (T_g), recrystallization endotherm temperature (T_c) and enthalpy (ΔH_c), melting endotherm temperature (T_m) and enthalpy (ΔH_f). Endothermic transitions are down (adapted from [42]).

1.7.4 Dielectric Relaxation Spectroscopy (DRS)

Dielectric Relaxation Spectroscopy (DRS) allows the determination of time dependency and intensity of electric polarization processes. This is done by taking a material and measuring its rate and extent of polarizability under a weak and oscilating electric field. The polarization of the material is manifested by the ability of the material's electrical charge storage and correlates with the environment, structure and mobility of charged molecular groups [43].

At lower frequencies, molecular dipoles will reorient in a field in order to decrease the electrical potential energy of the material, and follow the alteration of the field frequency. Although, at high enough frequencies the reorientation of dipolar molecular is unable to keep up with the alternating field and the dipoles relax back to their orientation. The range of frequencies in which molecules relax will partly depend on the environment and interactions with other close molecules. As a consequence, molecular dynamics and interactions can be investigated [43] [44].

The measure of charge needed to generate a field in a specific medium is permittivity (ε^*), and associated with the stored energy in the dielectric material is the real part of permittivity (ε'). The imaginary part of permittivity (ε'') is associated with the dissipated energy from the dielectric material. This value is always greater than zero, and the higher it is, the more energy is being lost from the system. The complex dielectric permittivity is given by the following equation:

$$\varepsilon^*(\omega) = \varepsilon'(\omega) - i\varepsilon''(\omega) \tag{1.1}$$

where ε' is the real part of complex permittivity, ε'' the imaginary part and ω the angular

frequency of the applied electric field.

One advantage of DRS over other techniques used to study water is the ability to differentiate the rotational ability of hydration water and free water. In the analysis of water, the dipoles of hydration water relax at frequencies of about 10^3 Hz whereas the dipoles of bulk water relax at frequencies close to 2 X 10^{10} Hz (at 25°C). This feature is very important as the rotational and translational mobility of water determine its availability and affect factors such as the physico-chemical stability of the material [43].

1.7.5 Nuclear Magnetic Resonance (NMR)

Nuclear Magnetic Ressonance (NMR) is one of the most general structural tools and one of the few techniques that can be applied to all states of matter. NMR takes advantage of the magnetic properties of certain nuclei, by exposing them to an external magnetic field and observing the transitions between spin states [45]. Solid-state NMR is commonly used to characterize nanomaterials, specifically ones that are functionalized. ^{29}Si ss-NMR in particular can reveal the structure of the material and its ligands. There is however a potential setback. To carry out these experiments, the sample has to be a dried powder, which in itself is not a problem, but when dealing with drug delivery data of these samples in an aqueous condition is needed.

Solution-state NMR is the tool needed to circumvent these issues. By having the samples wanted for analysis prepared in a solution, not only are the previously mentioned drawbacks fixed, but even further studies can be carried out. At a larger scale, it can be possible to investigate protein-ligand interactions and it is a critical tool for multiple steps in drug discovery [46]. One other application of this technique that will be relevant for this thesis is the use of solution-state NMR for functional group quantification in mesoporous silica [47].

1.7.6 Ultraviolet-visible Spectroscopy

Ultraviolet-Visible (Uv-Vis) spectroscopy takes advantage of the interactions of electromagnetic radiation, in the ultraviolet-visible region, and matter. The regions of interest in the electromagnetic spectrum are the ultraviolet (UV) region, ranging from 10 to 380 nanometers, and the visible region from 380 to 750 nanometers. Measurements can be taken in three different modes: reflectance, transmittance and photoluminescense. The first two modes need to be measured against a reference [48].

An electronic transition in the structure of a molecule or ion is needed for it to exhibit adsorption in the visible/ultraviolet region. This adsorption occurs with an alteration of the electronic state of the molecule, where electrons are promoted from a ground state orbital to an excited state or anti-bonding orbital by energy supplied by light. This spectroscopy allows for quantitative analysis, determination of dissociation constants of acids and bases and many other applications [49].

1.8 Main Goals of Thesis

The role of pore functionalization in mesoporous silica on the release profile of pharmaceutical compound efavirenz has not been studied. The aim of this thesis was to stabilize the amorphous state of the drug and gain a better understanding of how modifying the pore surface with aminopropyl, methyl and mercaptopropyl groups will affect the interactions between silica and drug, and furthermore, its release from the matrix.

1.9 Thesis Outline

The first chapter of this thesis will first acknowledge the issue of low water solubility of many drugs and explore related concepts. Additionally, there will be an overview of techniques used in the work. The second chapter contains the entire work methodology, from synthesis to sample characterization, and all parameters used in the analysis. In the third chapter, the experimental results obtained will be displayed and discussed, from the bulk drug to unloaded and loaded silica. Correlations will be made in an attempt to rationalize the observed results. Finally, the conclusion will have an overview of the achieved results and main conclusions to deduce from this work.

2

Materials and Methods

2.1 Synthesis of MCM-41

The MCM-41 silica was synthesized following the method described by Grün et al [50]. Trimethyloctadecylammonium bromide (CTAB C_{18}) was used as template.

First, 2.56 g of the template was dissolved in 120 g of deionized water (0.055 mol L^{-1} solution) and then 10.46 mL of aqueous ammonia (0.14 mol, 25% wt) was added to the solution. After the template has dissolved, 10.94 mL of tetraethylorthosilicate (TEOS) (0.05 mol) was added slowly, drop by drop. The mixture was stirred for 1 h, at room temperature. The white precipitate was filtered and washed with 100 mL of deionized water. After drying at 100 °C for 20 h, the product was calcinated at 550 °C (rate: 1 °C/min) in air, and kept at this temperature for 5 h.

2.2 Funcionalization of MCM-41

The funcionalized MCM-41 silica was synthesized following the one-pot method described by Iliade et al [51]. To achieve the necessary funcionalizations, 3 different organosilanes were used. These were 3-Aminopropyl)triethoxysilane (APTES), Methyltrimethoxysilane (MTM) and 3-Mercaptopropyl)trimethoxysilane (MPTMS).

First, 0.785 g of CTAB (0.002 mol) was dissolved in 300 mL of deionized water. To this solution, 2.45 mL of a fresh NaOH solution (2 M) was added and the temperature was raised to 80 °C. Subsequently, 3.5 mL of TEOS (0.018 mol) and 0.002 mol of organosilane were added slowly and simultaneously and the solution stirred for 2 h. The white precipitate was filtered and washed with abundant deionized water and methanol, and dried at room temperature.

The organic template was removed by refluxing the product in HCl (37 %) and methanol at 50 °C. The solution was refluxed for 1 h, the solvent replaced and the process repeated again. Following the replacement of solvent, the solution refluxed for another 20 h. Finally, the product was filtered and washed with abundant deionized water and methanol and dried at 100 °C for 24 h.

Table 2.1: Organosilanes used in MCM-41 functionalization

Organosilane	Functional Group	Supplier	CAS	Purity (%)
APTES	R-$(CH_2)_3$-NH_2	Sigma-Aldrich	919-30-2	98
MTM	R-CH_3	Sigma-Aldrich	1185-55-3	95
MPTMS	R-$(CH_2)_3$-SH	Sigma-Aldrich	4420-74-0	95

2.3 Nitrogen Adsorption

For the unloaded silica, nitrogen adsorption isotherms were measured at -196 °C, with a Micromeritics ASAP 2010 instrument, in the Laboratório de Análises/Requimte of the Chemistry Department of NOVA University of Lisbon. In preparation for the analysis, the samples were outgassed at 120 °C under vacuum for 6 hours.

2.4 Elemental Analysis

Elemental analysis was performed for all unloaded silica by Laboratório de Análises/ Requimte of the Chemistry Department of NOVA University of Lisbon, in a Thermo Finnigan CE Instruments elemental analyzer, model Flash EA 1112, CHNS series. The following elements were analyzed: carbon (C), hydrogen (H), nitrogen (N) and sulfur (S).

2.5 Transmission Electron Microscopy (TEM)

The samples were analyzed by MicroLab - Electron Microscopy Laboratory, in Instituto Superior Técnico. The equipment used was a high-resolution electron microscope Hitachi 8100.

2.6 Differential Scanning Calorimetry (DSC)

DSC analysis was carried out for all samples: bulk efavirenz, unloaded and loaded matrices. This was done with a DSC Q2000, from TA Instruments Inc., operated under a nitrogen atmosphere with a flow rate of 50 mL/min. Samples of 3-5 mg were placed in a Tzero Pan and covered with Tzero Hermertic Lid. The pans are sealed before analysis and perforated to ease water evaporation. The thermal procedure used and respective masses are introduced in the software that controls the equipment. The data obtained was analyzed using the Universal Analysis 2000 software provided by TA Instruments Inc.

2.7 Efavirenz Loading

To incorporate efavirenz in the silica, it was necessary to remove any water or impurities present in the silica. This was achieved by placing the silica in glass cells and submitting

them to vacuum for 8 hours at 150 °C. After, the samples were left to cool down to room temperature.

The amount of efavirenz needed to fill about 30% of the pore volume was calculated using the silica's pore volume, obtained by nitrogen adsorption, and efavirenz's density (1.5 g/cm^3). The drug masses were dissolved in 3 mL of ethanol and added to the samples, with the glass cells still under vacuum. All resulting composites were recovered with the use of a rotary evaporator. Henceforth, the composites will be identified by the matrix in which efavirenz was loaded: EFZ:MCM-41, EFZ:NH_2-MCM-41, EFZ:CH_3-MCM-41 and EFZ:SH-MCM-41.

Table 2.2: Masses of unloaded silica and efavirenz in order to have a pore filling of 30%.

Sample	$Mass_{silica}$ (mg)	$Mass_{efz}$ (mg)
MCM-41	100.10	60.30
NH_2-MCM-41	100.71	91.40
CH_3-MCM-41	100.24	84.36
SH-MCM-41	100.44	59.19

2.8 Attenuated Total Reflectance Fourier Transform Infrared Spectroscopy (ATR-FTIR)

The infrared spectra were obtained with a *PerkinElmer UATR Spectrum Two*, equipped with a UATR sampling accessory, for the wavenumber range of 400-4000 cm^{-1} with a resolution of 1 cm^{-1} and 16 scans.

2.9 Dielectric Relaxation Spectroscopy (DRS)

The samples analyzed were placed between two gold-plated electrodes of parallel plate capacitors. Afterwards, the cell was placed on a BDS 1100 cryostat. The sample was submitted to a gas stream originating from the evaporation of liquid nitrogen, causing a temperature change. Temperature control was controled by Quatro Cryosystem. The dielectric measurements were carried out using the Alpha-N independence analyzer from NovoControl technologies GmbH, covering the frequency range from 0.1 Hz to 1e^6 Hz, and extending the temperature from -120 to 140 °C.

2.10 Ultraviolet-Visible Spectroscopy

The Uv-Vis spectra of the samples was measured between 190-400 nm in quartz cells by a Thermo Scientific Evolution 201 Uv-Vis.

2.11 Nuclear Magnetic Ressonance

The NMR data was collected on a *Bruker Avance III 400* spectrometer operating at 400 MHz. Samples were prepared by placing 5-10 mg of unloaded functionalized silica in 400 μL of D_2O/NaOH. The samples were sonicated for 1 h and the experiment was performed immediately after. A known amount of 1,3,5-trioxane was added as an internal standard.

2.12 Controled Release Experiments

The release studies were carried out in 200 mL of phosphate buffer with a pH of 7,4. These were maintained at a temperature of 37 °C and 100 rpm. 1 mL aliquots were removed and 1 mL of fresh buffer was added, at 1, 3, 5, 10, 12, 15, 20, 30, 45, 60, 90, 120, 180 min and 24, 48h. These were measured at a wavelength of 190-400 nm and perfomed in duplicate. A calibration curve was done to quantify the amount of efavirenz. Five solutions of efavirenz (0.1, 0.5, 1, 3, 5 and 10 mg/L) in phosphate buffer were prepared and the following equation was obtained:

$$\text{Abs}(240\,\text{nm}) = 0.0091[\text{EFZ}](\text{mg/L}) + 0.0033(r^2 = 0.999) \tag{2.1}$$

The calibration curve was calculated for two wavelengths of 240 and 291 nm and linearity was only obtained at 240 nm. These measurements were performed in triplicate.

3

Results and Discussion

3.1 Nitrogen Adsorption

N_2 adsorption-desorption isotherms are shown in figure 3.1. In table 3.1 the textural properties are summarized. The specific surface area was obtained through the linear portion of the Brunauer–Emmett–Teller (BET) method plot, the total pore volume through the Density Functional Theory (DFT) model and the pore diameter by the Barrett-Joyner-Halenda (BJH) desorption method.

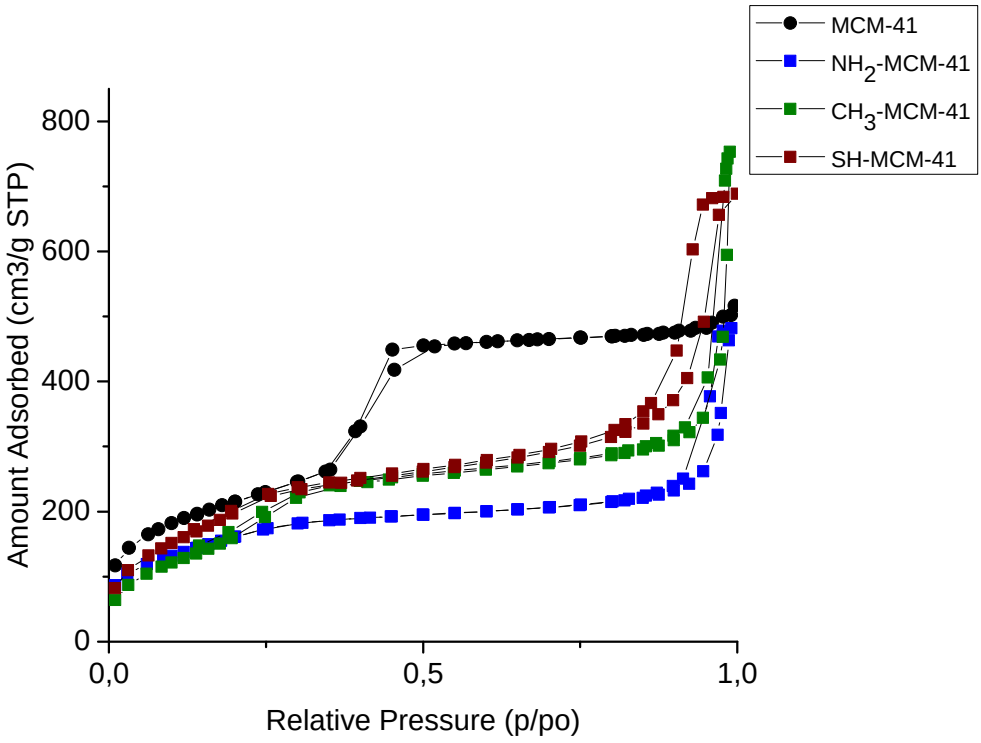

Figure 3.1: Nitrogen adsorption-desorption isotherms of MCM-41, NH_2-MCM-41, CH_3-MCM-41 and SH-MCM-41.

All samples present type IV (a) isotherms, characteristic of mesoporous materials [52]. The MCM-41 isotherm showed a type H1 hysteresis loop, typical of mesoporous

material with a uniform mesopore size distribution [53]. Additionally, the isotherm has the typical step in the 0.1-0.5 relative pressure range indicative of regular and well-ordered mesopores [53]. The functionalized samples exhibited a less defined step.

Table 3.1: Textural properties of unloaded silica.

Sample	Surface Area (m^2/g)	Total Pore Volume (cm^3/g)	Pore Diameter (nm)
MCM-41	783.6	0.746	3.40
NH_2-MCM-41	583.0	0.492	3.07
CH_3-MCM-41	618.0	0.532	2.98
SH-MCM-41	766.0	0.760	2.69

Given the values in table 3.1, there is a decrease of all three properties. This decrease derives from the less available space for adsorbed nitrogen corroborating the modification of the internal pore wall [54].

3.2 Attenuated Total Reflection Fourier Transform Infrared Spectroscopy (ATR-FTIR)

ATR FTIR spectra were used not only to analyze the MCM-41 silica but also the functionalizations made posteriorly. For this aim, several regions of the spectra are of importance. This first region, from 4000-3500 cm^{-1}, is where the surface silanol groups will be detected. The second region, from 3500-1200 cm^{-1}, will show the presence of methyl groups. The last region, from 1500-400 cm^{-1}, has different types of vibrations for the Si-O-Si group [55]. In the first region pertaining to the unmodified silica, from 4000-3500 cm^{-1}, (see figure 3.2), no band corresponding to the silanol group is visible.

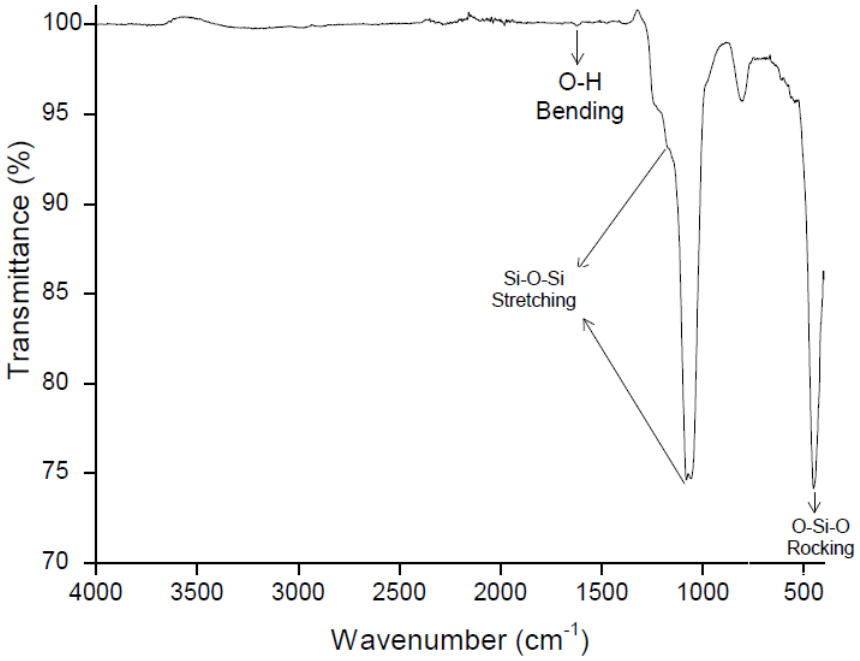

Figure 3.2: ATR-FTIR spectra of the unmodified silica.

In the next range, from 3500-1200 cm^{-1}, the presence of surface hydroxyl groups or water is not very clear due to the absence of the typical broad band, although there is a small band at 1625 cm^{-1}, possibly from the O-H bond bending of molecular water[56]. Also, the Si-CH_3 bond vibration is evident at 1376 cm^{-1}. In the last region, the asymmetric and symmetric stretching of Si-O-Si bonds are present at 1242 and 1063 cm^{-1}, respectively, and the symmetric stretching appears at 806 cm^{-1}. The band at 963 cm^{-1} results from the Si-OH bond stretching. Lastly, at 449 cm^{-1} there is the O-Si-O bond rocking.

Moving on to the first modified silica with the aminopropyl group (NH2-MCM-41), it is possible to observe that both silicas have the same bands between 1500-400 cm^{-1}, although with different intensities, evidence of their similar composition (see figure 3.3).

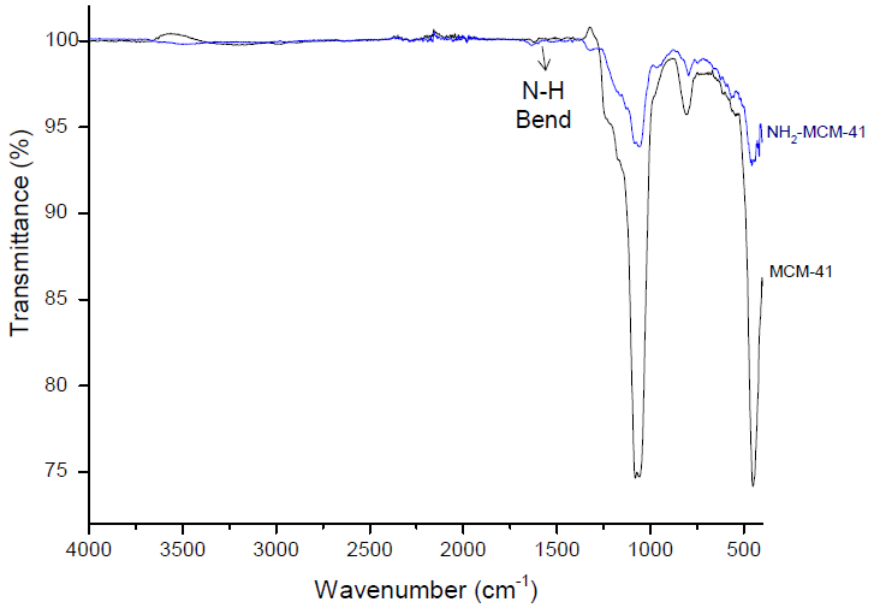

Figure 3.3: ATR-FTIR spectra of the MCM-41 (black) and NH_2-MCM-41 (blue) silica.

At first, the surface group modification does not seem apparent given the absence of N-H stretch bands at around 3300 cm^{-1}. However, there is a band at 1523 cm^{-1} from the N-H bend of the primary amine.

For the second modified silica, with methyl groups (CH_3-MCM-41), more visible changes are immediate in the spectra, besides the base groups (see figure 3.4). For this silica, the silanol groups are much more apparent as seen by the broad band at about 3260 cm^{-1}.

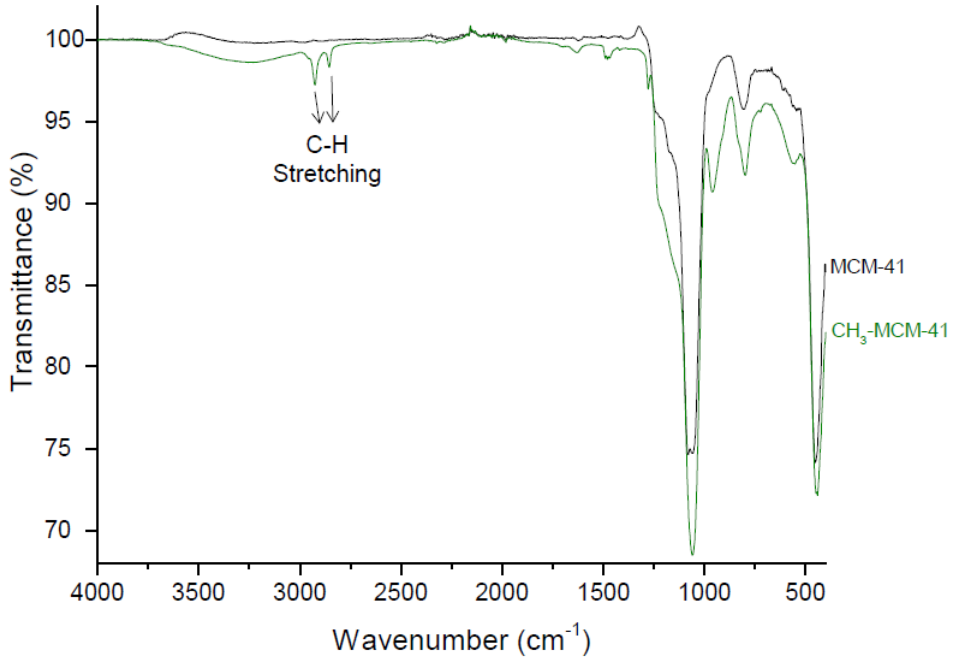

Figure 3.4: ATR-FTIR spectra of the MCM-41 (black) and CH_3-MCM-41 (green) silica.

A closer look at the 3000-1400 cm^{-1} region lets us observe the methyl presence, evident by the sharp bands at 2924 and 2853 cm^{-1} from the asymmetric and symmetric stretching of the C-H bond, respectively. The remaining bands coincide with the base structure of the silica and have been previously identified.

Finally, the last modified silica has mercaptopropyl groups on the pore surface (see 3.5). These groups have two signals on the spectra, one at 2900 cm^{-1} for the C-H stretching vibrations of the propyl chains and another weaker signal at 2580 cm^{-1} for the S-H bond. These signals are not very apparent in the spectra.

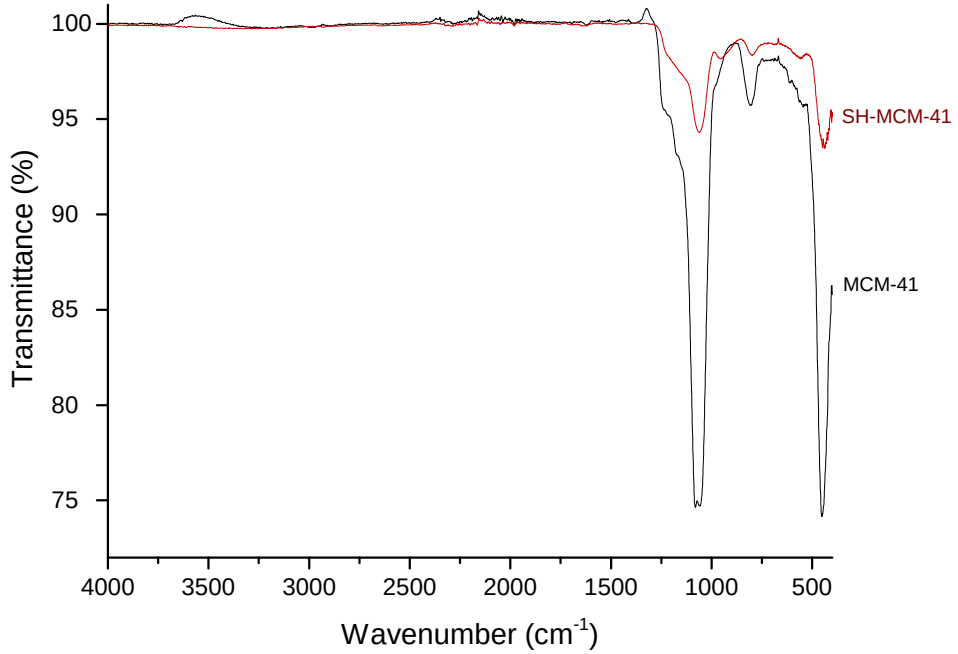

Figure 3.5: ATR-FTIR spectra of the MCM-41 (black) and SH-MCM-41 (red) silica.

3.2.1 Efavirenz

Efavirenz displays several characteristic bands (see figure 3.6), the first at 3303 cm^{-1} due to the N-H stretching vibration followed by a band at 2251 cm^{-1} from the stretching vibration of the carbon triple bond. There is also the C=O stretching vibration at 1745 cm^{-1} and the stretching vibrations of the aromatic C=C bonds at 1601 and 1495 cm^{-1}. Finally, at 1185 cm^{-1} there is the stretching vibration of the C-F bonds and at 1040 cm^{-1} the C-Cl stretching vibration [57]. The bands expected to be observed in the FTIR spectra of the composites are located at 3303, 2251 and 1745 cm^{-1}.

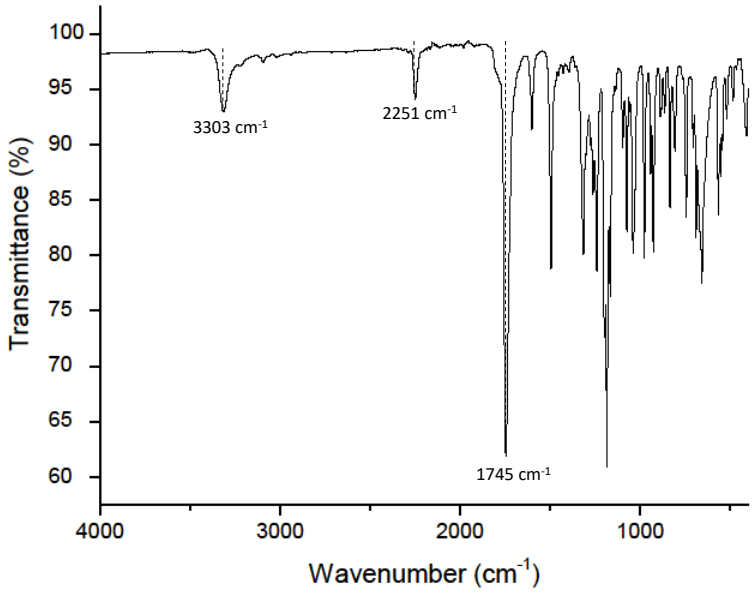

Figure 3.6: ATR-FTIR spectra of efavirenz.

3.2.2 Loaded Silica

ATR-FTIR was used to determine qualitatively if the drug was incorporated into the silica. We can see that in all the silica (see figure 3.7) the presence of efavirenz is evident given that all the main bands of the drug are present. In the EFZ:MCM-41 silica the N-H stretching vibration band is absent, and in its place there is a broad band between 3000 and 3500 cm^{-1}. This band is likely due to the presence of adsorbed water in this silica [58].

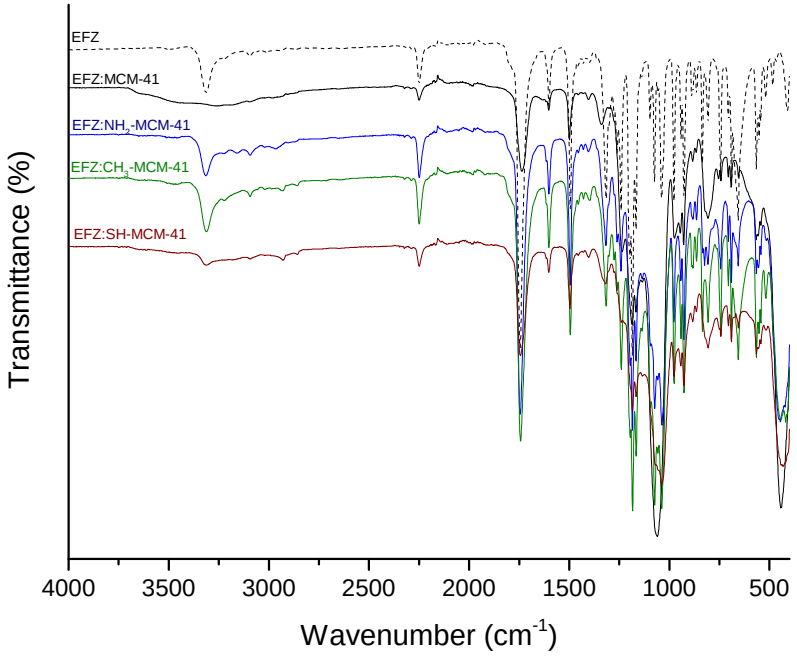

Figure 3.7: ATR-FTIR spectra of bulk efavirenz (dotted black), EFZ:MCM-41 (black), EFZ:NH_2-MCM-41 (blue), EFZ:CH_3-MCM-41 (green) and EFZ:SH-MCM-41 (red) samples. All curves were vertically displaced for a better visualization.

Furthermore, in the EFZ:NH_2-MCM-41 and EFZ:CH_3-MCM-41 samples there is a higher peak intensity and signal broadening at around 1000 cm^{-1} due to the overlap of the characteristic bands of MCM-41. This intensity could be an indication of efavirenz present on the outside of the pores. With other techniques further on in this project, this conjecture will be clarified.

3.3 Elemental Analysis

Table 3.2: Mass percentages of nitrogen, carbon, hydrogen and sulfur in all four synthesized silica.

Sample	Nitrogen (%m/m)	Carbon (%m/m)	Hydrogen (%m/m)	Sulfur (%m/m)
MCM-41	0,00	0,01	0,40	0,00
NH_2-MCM-41	1,09	3,52	1,96	0,00
CH_3-MCM-41	0,65	14,48	3,04	0,00
SH-MCM-41	0,29	14,16	2,71	6,27

Elemental analysis enabled the determination of the elements present in the unloaded silica, extremely helpful to help determine if the surface group modification was successful.

With the MCM-41 silica there is no presence of nitrogen, since the surfactant was fully removed by calcination. SH-MCM-41 shows the existence of sulfur, which confirms the successful incorporation of mercaptopropyl groups that had not been possible with ATR-FTIR. Additionally, there is nitrogen in both SH-MCM-41 and CH_3-MCM-41 that should not be present. Once again, this nitrogen originated from the surfactant and was not removed fully from the samples. Finally, the NH_2-MCM-41 has nitrogen as expected.

The sample treated with MPTMS allows for calculations to infer the amount of surfactant remaining. Considering 100 grams as a reference for the calculations, 6.27 % of sulfur correspond to 0.196 mol. Taking into account that one atom of sulfur is connected to three atoms of carbon, 0.588 mol of carbon are due to the functional group, that is, 7.05 % of the remaining amount of carbon in the sample is likely due to surfactant or solvent used during the synthesis.

Using the same course of thought for CH_3-MCM-41, it is also possible to calculate the amount of surfactant on this sample, since all nitrogen present must derive from the surfactant. The 0.65 % of nitrogen corresponds to 0.046 mol. Given that for every one atom of nitrogen, on the surfactant, there are nineteen carbon atoms, that is, 10.59 %. Therefore, 3.89 % of carbon present in this sample derived from the organic modification. Considering these results, it can be concluded that the incorporation of functional groups was successful, particularly considering the initial amount of organosilane added in the synthesis.

3.4 Nuclear Magnetic Ressonance (NMR)

The samples were further characterized by ^{1}H NMR as reported by Cruncho et al. [47]. This method requires an internal standard, trioxane, to be used in quantification. The amount of organic molecules grafted onto the surface of pores can be estimated using the peaks of the protons from the alpha-carbon to the silicon atom, by comparing their integrated intensities with the internal standard. The ^{1}H NMR spectra for the three functionalized silica nanoparticles are presented in the following figures:

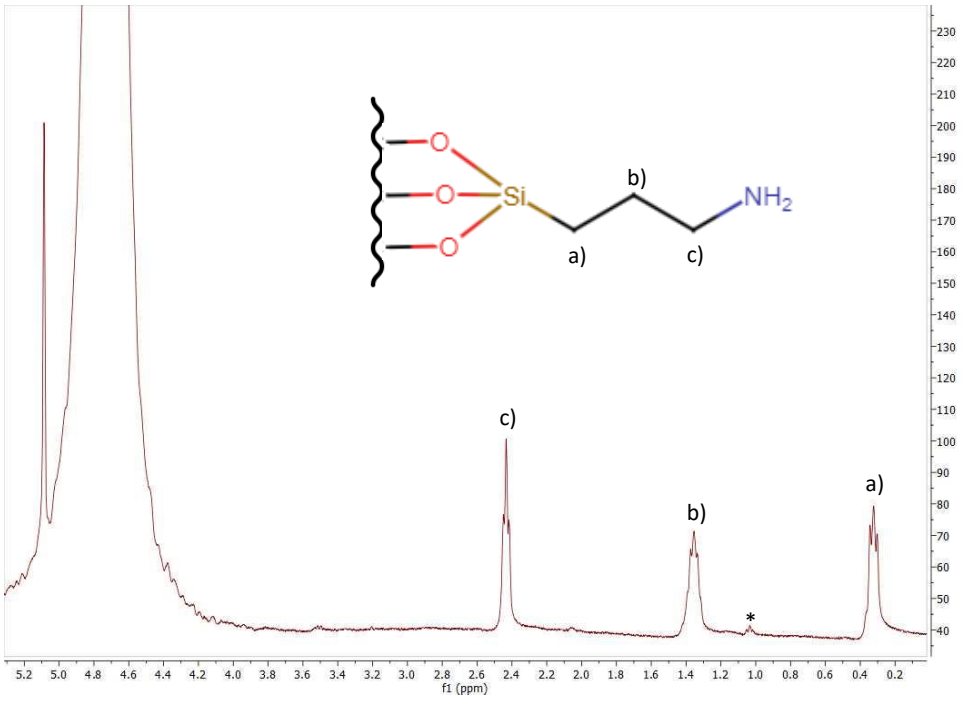

Figure 3.8: ^{1}H NMR spectra for NH_2-MCM-41 in $NaOH/D_2O$. The internal standard peak is at 5.09 ppm. CTAB peak is marked with (*).

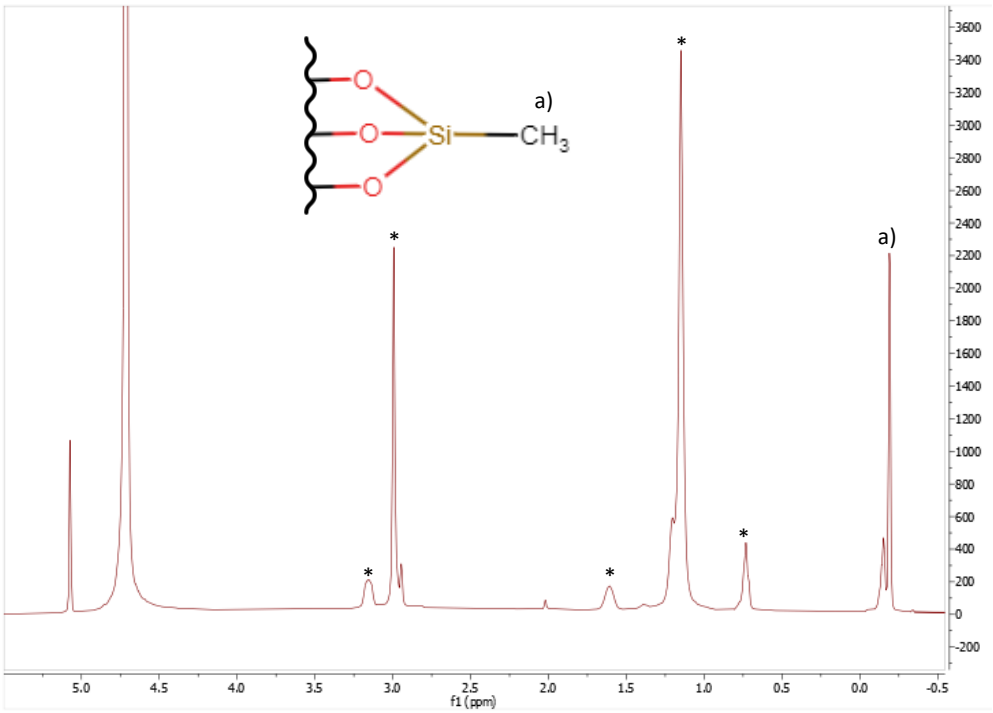

Figure 3.9: ^{1}H NMR spectra for CH_3-MCM-41 in $NaOH/D_2O$. The internal standard peak is at 5.07 ppm. CTAB peaks are marked with (*).

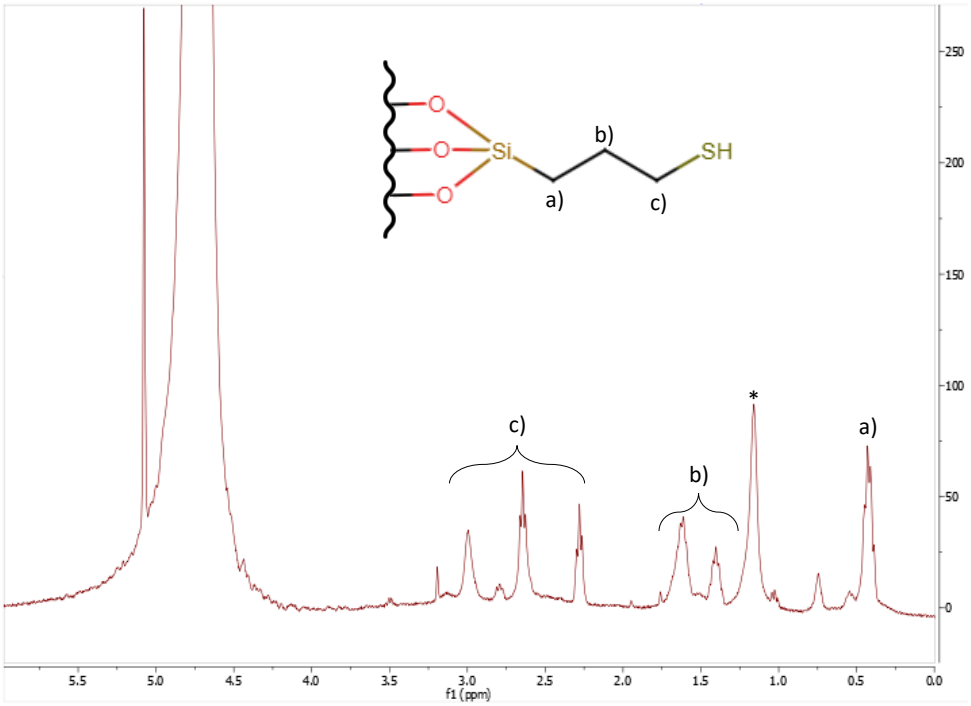

Figure 3.10: ^{1}H NMR spectra for SH-MCM-41 in NaOH/D_2O. The internal standard peak is at 5.07 ppm. CTAB peak is marked with (*).

In all the samples, the internal standard peak is present at about 5.07 ppm and the peaks associated with the distinct organic groups are present and have been associated with atoms in the respective structure. Additionally, there are also peaks pertaining to trimethyloctadecylammonium bromide (CTAB). This was expected given that in section 3.3, pertaining to elemental analysis results, all modified silica was shown to have traces of surfactant, incompletely removed after synthesis. The surface group quantification was not possible, given that the particles are not spherical. A model that more accurately describes the particle's shape would need to be used in order to obtain accurate values.

3.5 Transmission Electron Microscopy (TEM)

The mesoporous structures of unloaded MCM-41 silica and its modified counterparts were examined by TEM images as shown below:

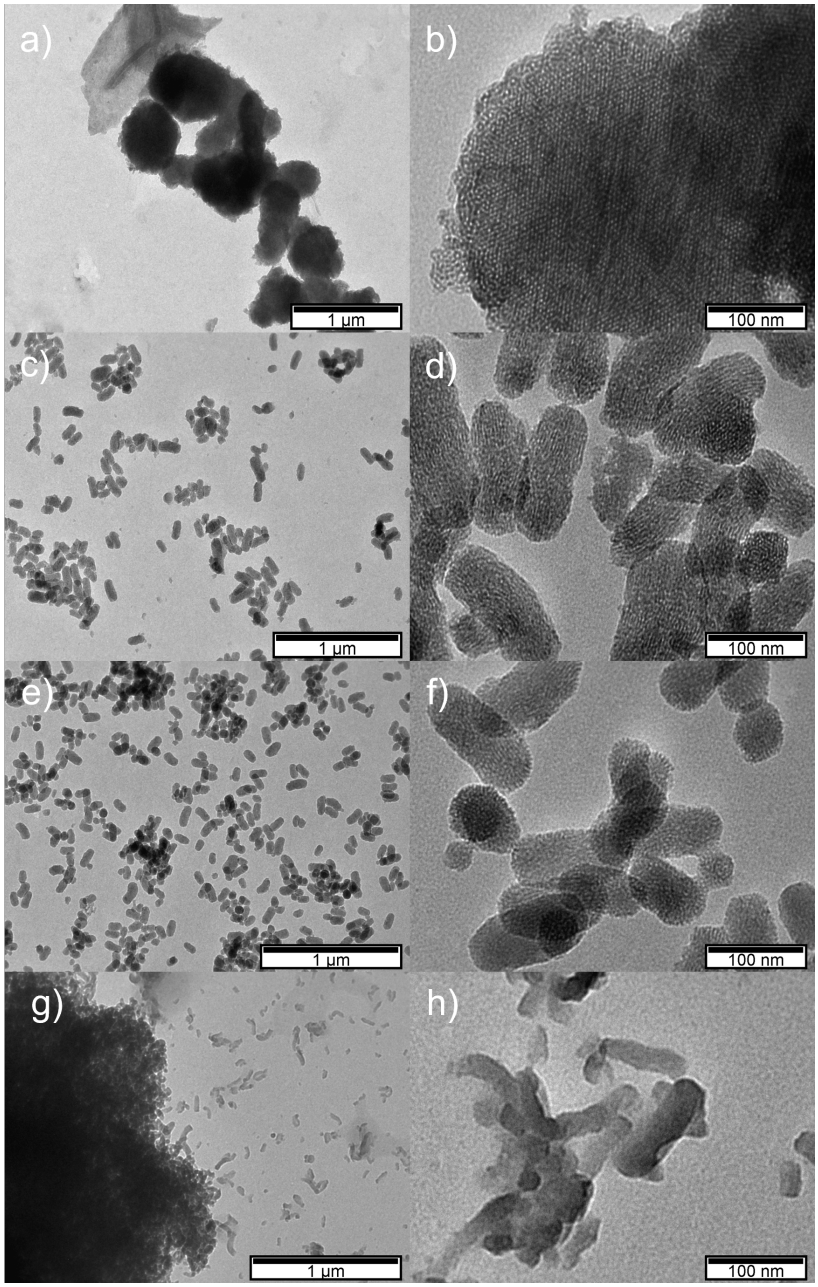

Figure 3.11: TEM images of MCM-41 (a, b), NH_2-MCM-41 (c, d), CH_3-MCM-41(e, f) and SH-MCM-41 (g, h).

These images revealed the different particle size and shapes. The MCM-41 silica shows an irregular shape, with the biggest particle size. All modified silica took the shape of rods but with different sizes, NH_2-MCM-41 being the biggest and SH-MCM-41 the smallest. All the silica present straight mesoporous channels with the exception of SH-MCM-41 in which it is not possible to observe the presence of these channels, due to the small particle size. The particle measurements were analyzed using the *ImageJ* software. Given that the obtained particles are not spherical, the values obtained were length and height (see table 3.3).

Table 3.3: Average values of length and height for syntheses mesoporous silica.

Sample	Length (nm)	Height (nm)
MCM-41	523	591
NH_2-MCM-41	70	143
CH_3-MCM-41	62	119
SH-MCM-41	26	110

3.6 Differential Scanning Calorimetry (DSC)

3.6.1 Determination of melting and glass forming possibility

Upon heating the fresh sample up to 155 °C, the DSC thermogram obtained shows an endothermic peak that corresponds to the melting of efavirenz (see figure 3.12), with an enthalpy variation of ΔH_m=52.15 J/g and temperature of T_m=137.7 °C. These values are in accordance with literature [59], in particular polymorph I characterized by Fandaruff et al [22].

In the subsequent cooling, the exothermic peak of crystallization is not observed. Since at around 35.15 °C the step associated with the glass transition is observed, it can be concluded that all of the sample was vitrified. Following the glass transition, no cold crystallization is observed. Ramos et al [60] reported an exothermic cold crystallization signal, starting at 70 °C and ending at 110 °C, for heating rates between 2 °C and 10 °C min^{-1}, and no crystallization was observed during cooling. Given this, efavirenz exhibits a good glass forming ability that is well observed in these results.

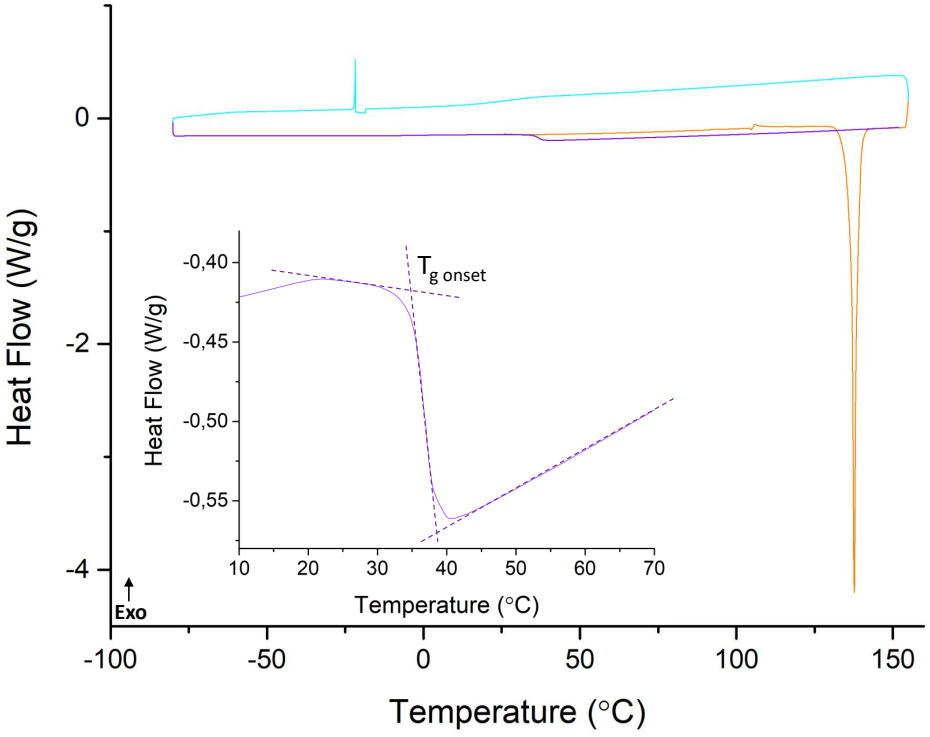

Figure 3.12: DSC thermograms of bulk efavirenz at 10 °C/min: (i) during heating, from 25 °C to 155 °C(orange);(ii) during cooling, from 155 °C to -80 °C(light blue); (iii) during heating, from -80 °C to 155 °C(purple). The glass transition region on heating was enlarged in the inset (mass = 2.86 mg).

3.6.2 Determining the necessary conditions for cold crystallization

To analyze the conditions in which efavirenz crystalizes, two more studies were conducted. In the first one, the sample was subjected to cooling at 10 °C/min from 155 °C to several final temperatures in order to determine the minimal temperature needed for the crystallization (see scheme in the inset of figure 3.13). Five final temperatures were investigated: 40, 20, 0, -20, -40 and -60 °C. The presence of the glass transition on both the cooling (at 10 °C/min) and the heating (at 5 °C/min) steps was detected in all cycles (temperature of T_{gonset}=33.0±0.2 °C).

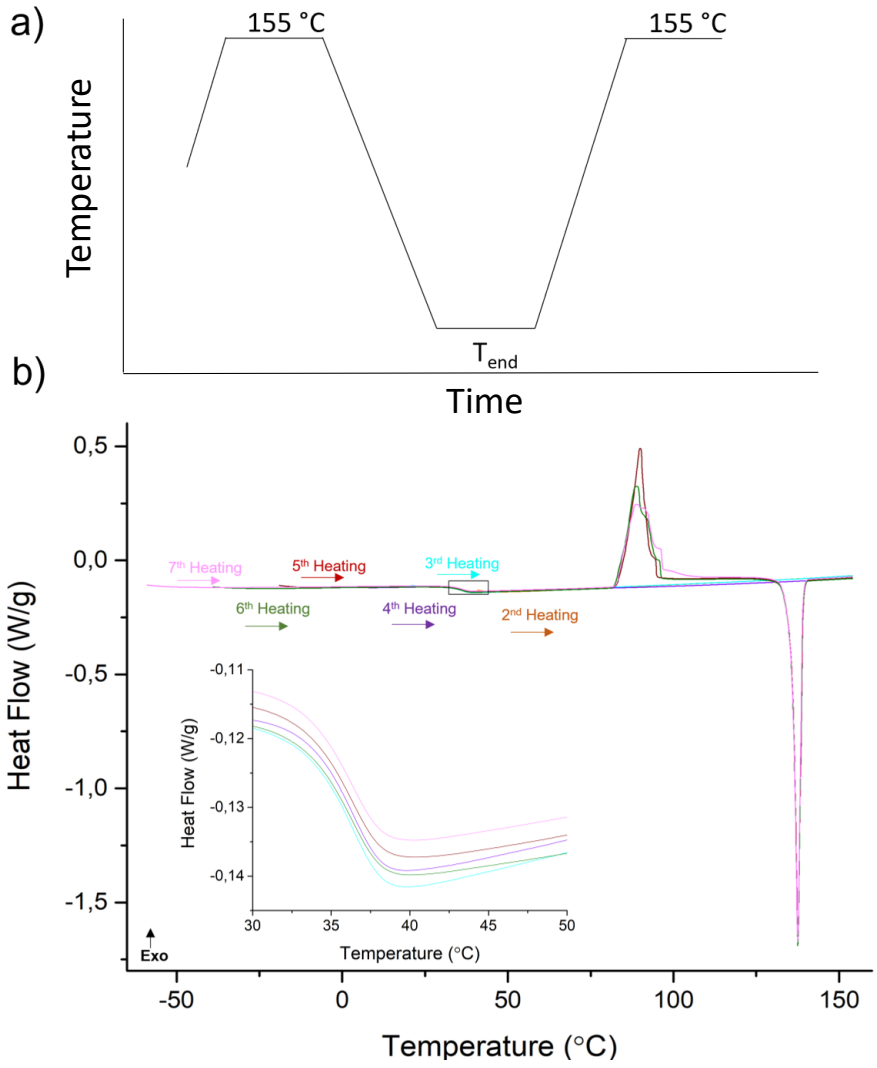

Figure 3.13: C(a) Experimental procedure followed; (b) DSC thermogram of bulk efavirenz during heating at 5 °C/min after previous cooling at 10 °C/min down to different temperatures (T=40, 20, 0, -20, -40, -60 °C). The glass transition region was enlarged (mass=3.81mg).

The thermogram shows that crystallization was only observed for 3 of the 6 temperatures. Cooling the sample to -20, -40 or -60 °C led to the appearance in the heating thermogram of the characteristic exothermic peak of the cold-crystallization (T_c=81.69 °C) followed by melting (see figure 3.14 where the complete cycle with T_{end}=-40 °C is represented as an example). This therefore led us to conclude that -20 °C is the minimum temperature needed to induce the cold crystallization of EFZ at 5 °C/min.

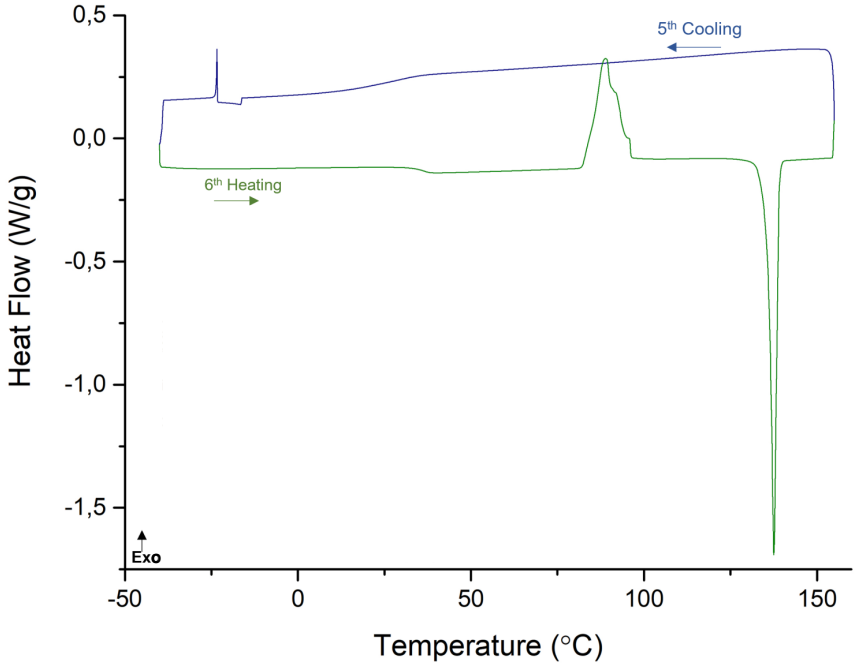

Figure 3.14: DSC thermograms of bulk efavirenz at 10 °C/min: (i) during cooling, from 155 °C to -40 °C (blue); (ii) during heating, from -40 °C to 155 °C (green).

While the crystallization temperature remained almost constant across the 3 T_{end} (table 3.4), the enthalpy of crystallization increased slightly with the decrease in the end temperature. Attending to the melting temperature observed in the three final cycles, T_m=137.55±0.01 °C, we can also conclude that the same polymorph of the initial sample was obtained.

Table 3.4: Values calculated from DSC thermogram displayed in figure 3.13 relative to glass transition, crystallization and melting.

			Crystalization		Melting	
T_{end} (°C)	T_g (°C)	ΔC_p (J/g·°C)	T_c (°C)	ΔH (J/g)	T_m (°C)	ΔH (J/g)
40	-	-	-	-	-	-
20	33,8	0,27	-	-	-	-
0	32,9	0,31	-	-	-	-
-20	32,7	0,32	89,9	36,4	137,6	44,9
-40	32,7	0,31	88,8	37,1	137,5	45,5
-60	32,8	0,31	88,8	38,4	137,6	44,7

From the crystallization enthalpy calculated, it was possible to estimate the crystalline fraction obtained by the following equation:

$$\%\text{Crystallization} = \frac{\Delta H_m(T_{end})}{\Delta H_m(\text{InitialExperiment})} \times 100 \tag{3.1}$$

where ΔH_m (T_{end}) is the value of the melting enthalpy for the T_{end} chosen and ΔH_m (Initial Experiment) corresponds to the value of ΔH_m=52.15 J/g, pertaining to polymorph I as determined in section 3.6.1 . It is important to remember that this equation can only be used to compare data about the same polymorph. Given this, the percentage of crystalline sample in this study was % Crystallization=86.4 ±0.2 %.

With the previous data, we can conclude that necessary requirements for the crystallization of efavirenz from the liquid state are as follows: cooling to a temperature equal or below than -20 °C and then heating above 80 °C at 5 °C/min.

3.6.3 Investigating isothermal crystallization

With the crystallization conditions established from the previous results, it was investigated the isothermal crystallization of EFZ. For this aim, the liquid sample (i.e. initializing above T_{fusion}) was subjected to a more complex protocol consisting in: (i) cooling down to -50 °C, (ii) heating up to 85 °C, (iii) isothermal during 1 hour, (iv) cooling down to -50 °C and finally (v) heating again up to 155 °C. All the ramps were at 10 °C/min. This thermal procedure is schematized in figure 3.15 a) .

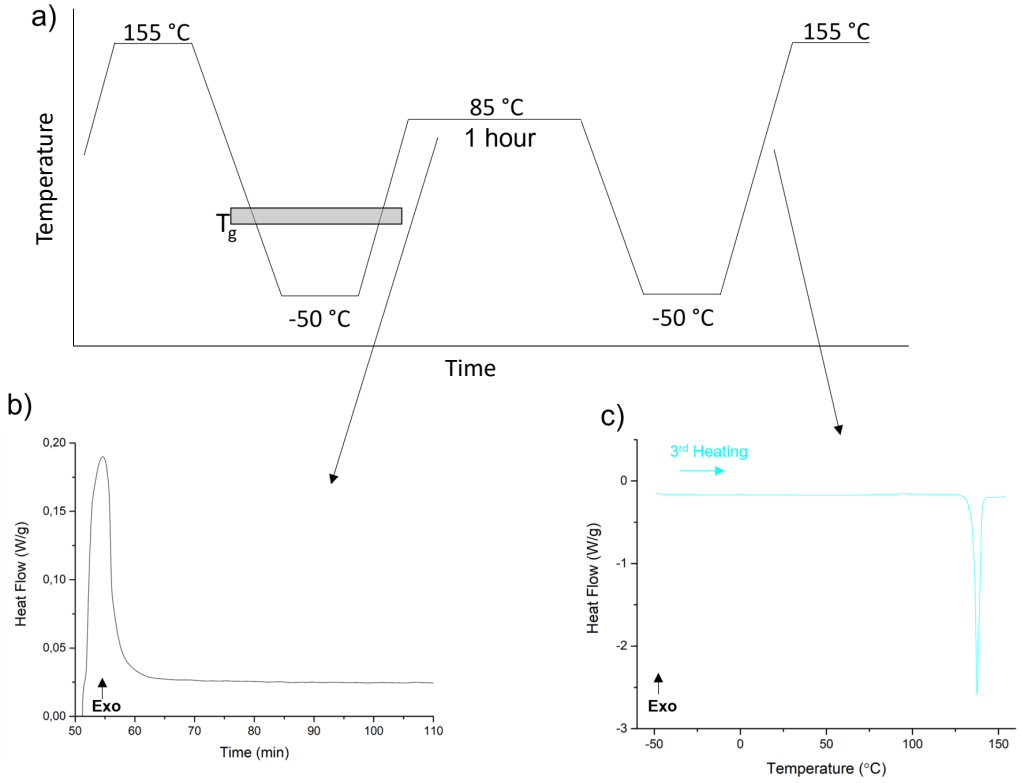

Figure 3.15: (a) Experimental procedure followed; (b) Thermogram obtained during the isothermal at 85 °C (ΔH_m=36.83 J/g); (c) Thermogram obtained on heating at 10 °C/min after isothermal crystallization at 85 °C (mass=3.81 mg).

The variation of heat flow with time during isothermal step (see figure 3.15 b)) shows an endothermal peak initializing as soon as the temperature stabilizes, corresponding the crystallization of EFZ. The enthalpy equals ΔH=36.83 J/g. It can be noticed that the end of the peak occurs just around 10 minutes, indicating that the recrystallization attains the maximum at this temperature. Upon heating after isothermal crystallization (see figure 3.15 c)), a small step is observed around 30 °C which would be compatible with the glass transition signal (see figure A.1).

Given that the melting temperature in this study is T_m=137.53 °C, we can conclude that this is the same crystal present in the fresh sample analyzed (figure 3.12) due to the very similar temperatures (T_m=137.69 °C for the fresh sample). Considering this, it is possible to calculate the percentage of the sample that has crystallized using the enthalpy values of both studies using equation 3.1, which in this case is 92 %. This value is compatible with the detection of the glass transition, as previously commented.

3.6.4 Investigating crystallization kinetics

To better comprehend the crystallization kinetics of efavirenz, a more complex crystallization procedure was carried out: (i) cooling down to -50 °C at 10 °C/min, (ii) heating to crystallization temperature at 10 °C/min, (iii) isothermal during 2 hours, (iv) cooling to -50 °C at 20 °C/min and finally (v) heating up to 155 °C (see figure 3.16).

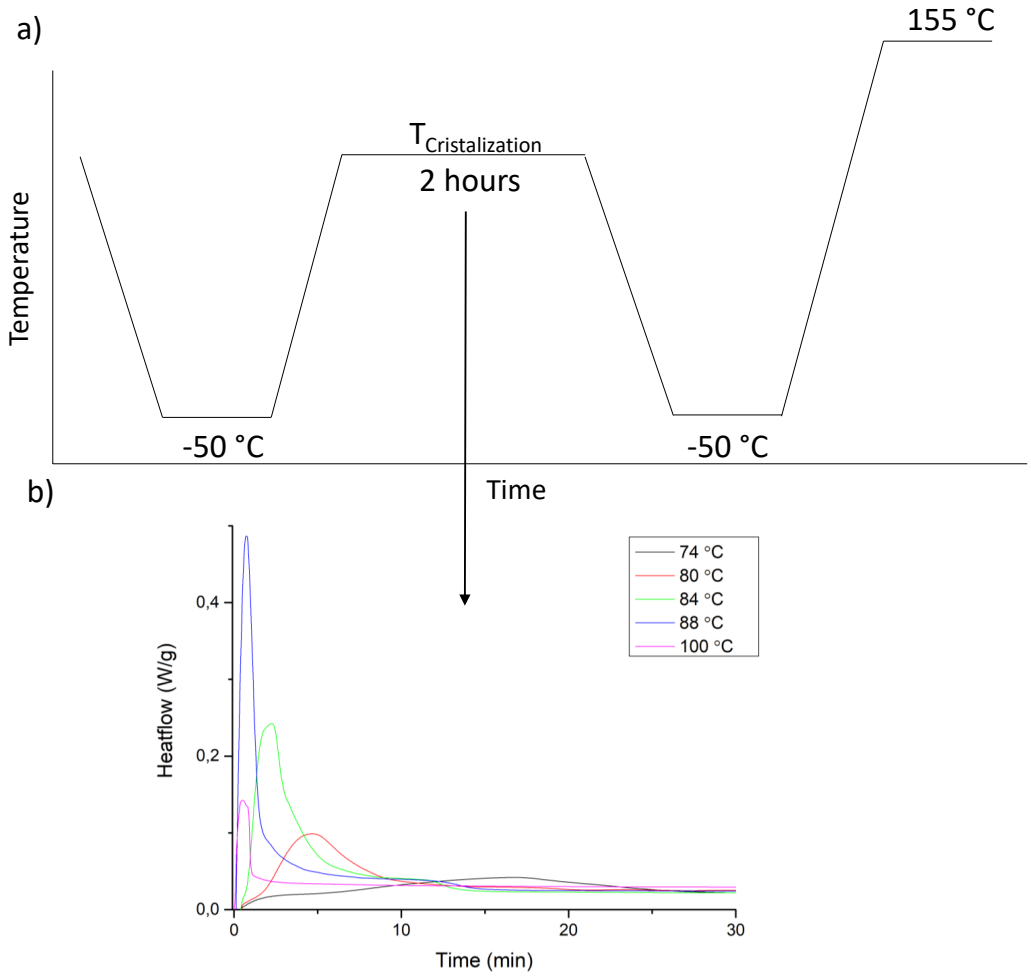

Figure 3.16: (a) Experimental procedure followed; (b) Thermogram obtained during the isothermals at 74 °C, 80 °C, 84 °C, 88 °C and 100 °C. All the isothermals were corrected to start at t=0 minutes. Only the first 30 minutes of the isothermals are represented for better visualization of the crystallization signal (mass=3.79 mg).

Taking into account the enthalpy values (see table 3.5), we can see that at T=84 °C there is the highest enthalpy value. There is also a trend with the time spans. As the temperature of crystallization increases, there is a decrease in the time interval in which the peaks occur. Not only that, at T=100 °C there is a crystallization peak before the isothermal even starts (ΔH=26.04 J/g). This is evidence that the efavirenz started to crystallize before the temperature stabilized.

Table 3.5: Values calculated from the previous DSC thermogram (figure 3.16) relative to glass transition, crystallization and melting.

			Crystalization	Melting	
Temp (°C)	T_g (°C)	ΔC_p (J/g·°C)	ΔH (J/g)	T_m (°C)	ΔH (J/g)
74	34,6	0,36	-	137,1	44,8
80	34,6	0,35	19,8	137,1	44,9
84	34,7	0,35	25,8	137,1	44,2
88	34,6	0,35	20,4	137,1	44,5
100	34,5	0,35	4,6	137,6	44,7

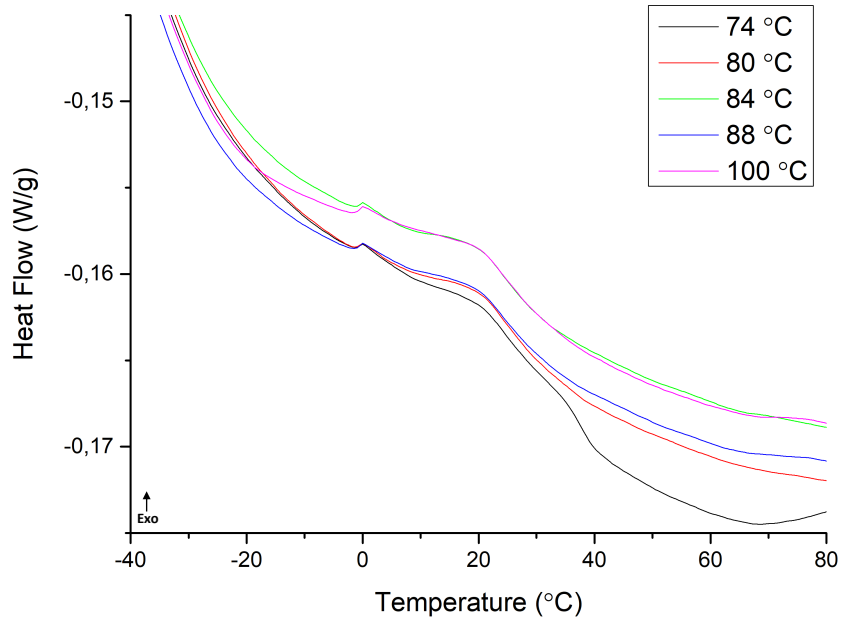

Figure 3.17: (a) Heating thermograms obtained at 10 °C/min after different isothermal crystallizations shown in figure 3.16 (mass=3.79 mg).

From the thermograms obtained on posterior heating (after isothermal crystallization), these show a similar T_g (see figure 3.17).Additionally, given the absence of any signals before melting and constant melting temperature throughout the cycles,it can be concluded that there is only one form of efavirenz in this study. Once again, using equation 3.1, the crystallization fraction can be calculated, which in this study is 86 %. Not only does this imply that different crystallization temperatures have no influence on the glass transition, more importantly it is not affected by the significant crystalline

fraction present in the sample.

3.6.5 Unloaded Silica

In the DSC thermogram of unloaded silica (fig 3.18) no thermal events are observed, aside from the endothermic peaks from the water removal during the first heating.

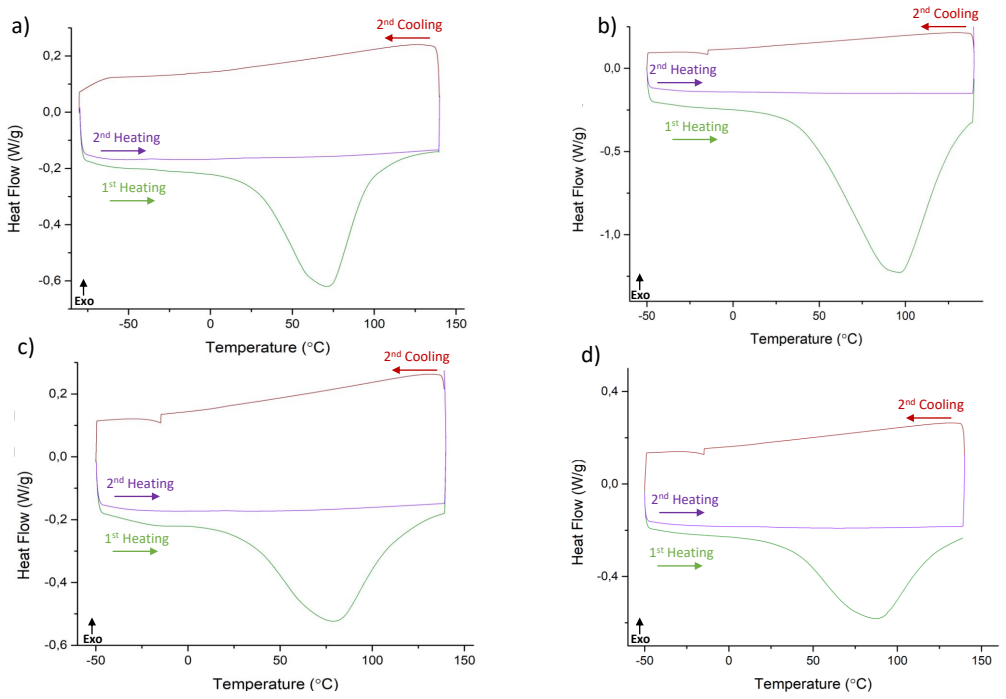

Figure 3.18: DSC thermograms of MCM-41 (a), NH_2-MCM-41 (b), CH_3-MCM-41 (c) and SH-MCM-41 (d) at 10 °C/min: (i) during heating, from -50 °C to 140 °C (green); (ii) during cooling, from 140 °C to -50 °C (red); during heating, from -50 °C to 140 °C (purple).

Different samples released different amounts of water, as seen in table 3.6. This water content was estimated from the weight loss between samples at room temperature and after the DSC run of figure 3.18. The unmodified silica loss the most substantial amount of water of all 4 samples. CH_3-MCM-41 presented the lowest water amount, in accordance with the hydrophobic nature of methyl groups [61].

Table 3.6: Percentage of water loss estimated by calorimeter drying.

Sample	ΔM (%) DSC
MCM-41	23
NH_2-MCM-41	11
CH_3-MCM-41	2
SH-MCM-41	4

3.6.6 Loaded Silica

Differential scanning calorimetry was used to study the physical state of efavirenz in MCM-41, NH_2-MCM-41, CH_3-MCM-41 and SH-MCM-41. The first sample, EFZ:MCM-41 (figure 3.19 a)), was submitted to two heating and cooling cycles, between -80 and 160 °C. In the first heating there is a broad peak with a minimum around 66 °C from water evaporation from the sample. Given that there is no evidence of the efavirenz melting peak, this suggests EFZ is inside the silica in the amorphous state. Additionally, the glass transition can be observed at T_g=22.6 °C.

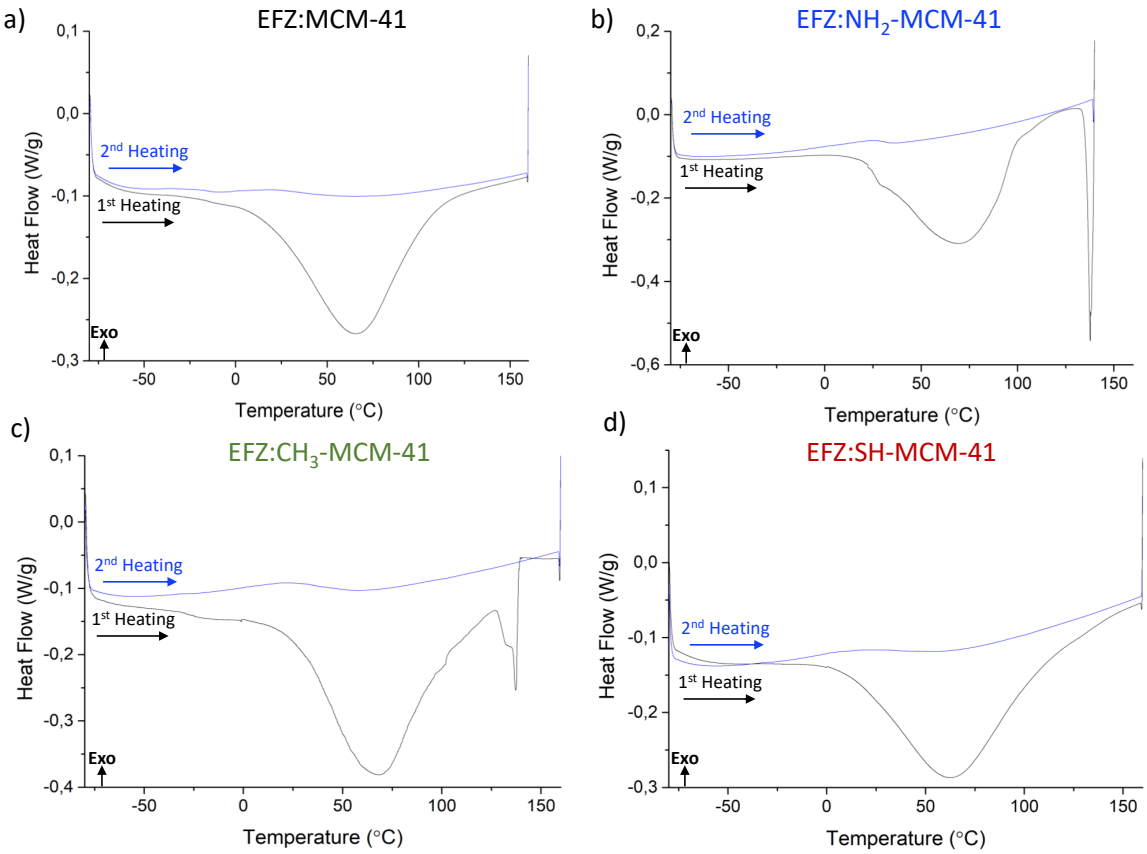

Figure 3.19: DSC thermogram of: a) EFZ:MCM-41 at 10 °C/min^{-1} (mass=4.33mg); b) EFZ:NH_2-MCM-41 at 10 °C/min^{-1} (mass=4.28mg); c) EFZ:CH_3-MCM-41 at 10 °C/min^{-1} (mass=4.41mg); d) EFZ:SH-MCM-41 at 10 °C/min^{-1} (mass=3.80mg).

EFZ:NH_2-MCM-41 (figure 3.19 b)) was also submitted to two heating and cooling cycles, between -80 and 140 °C. Once more, there is water evaporation in this sample, with a minimum around 70 °C. After the water release, melting is always observed at the same temperature of native efavirenz, evidence of the presence of EFZ outside the pores. In both heating cycles, glass transition is present, T_g=27.0 °C, an exhibit of efavirenz amorphization [62].

EFZ:CH_3-MCM-41 (figure 3.19 c)) shows several thermal events in the first heating

cycle. Firstly there is water removal, with a minimum around 68 °C. Secondly, there is a melting endotherm with two peaks, at T_m=132.7 °C and T_m=137.1 °C. The second peak coincides with the melting of efavirenz. The first peak possibly originates from melting of a crystalline fraction of efavirenz inside the pores. Yet again, the glass transition is observed in the second heating cycle at T_g=26.5 °C.

The last composite, EFZ:SH-MCM-41 (figure 3.19 D)), exhibits a similar behavior to EFZ:MCM-41. Not only is there water loss, with a minimum around 63 °C, but the only other thermal event is the glass transition in the second heating cycle at T_g=23.6 °C. Further more, the water loss percentage and glass transition range are very similar for both of these samples. Since it has been observed that EFZ:NH_2-MCM-41 and EFZ:CH_3-MCM-41 have efavirenz present ouside their pores, this evidence correlates with the higher relative intensity of their correspondent FTIR spectra in figure 3.7. From the

Table 3.7: Glass transition temperature at onset, midpoint and endpoint, and percentage of water loss for all four composites.

Sample	T_{g-on} (°C)	T_{g-mid} (°C)	T_{g-end} (°C)	ΔM (%)
EFZ:MCM-41	22.6	36.8	45.3	5
EFZ:NH_2-MCM-41	27.0	31.5	34.0	5
EFZ:CH_3-MCM-41	26.5	35.3	51.4	8
EFZ:SH-MCM-41	23.6	34.7	42.5	4

analysis of the previous thermograms, it is possible to conclude that all four silica appear to stabilize the amorphous state of efavirenz. In addition, NH_2-MCM-41 and EFZ:CH_3-MCM-41 show evidence of the drug outside the silica's pores. It is also important to look at the glass transition values.

When compared to bulk efavirenz, with a glass transition wideness of ~ 7 °C (thermogram of efavirenz taken at 10 °C/min^{-1} in figure 3.12), all composites, with the exception of EFZ:NH_2-MCM-41, have significantly broader glass transitions between ~ 19 (EFZ:SH-MCM-41) and ~ 24 °C (EFZ:CH_3-MCM-41). In the case of EFZ:NH_2-MCM-41, the wideness is the same although the glass transition temperature has shifted to lower temperatures, when compared to bulk efavirenz. Given that the matrices differ in functional groups present at the surface, these clearly alter the environment of confined EFZ, leading to altered physical properties.

3.7 Dielectric Relaxation Spectroscopy (DRS)

3.7.1 Efavirenz

Dielectric relaxation spectroscopy measurements were taken to analyze the behavior of efavirenz and characterize the amorphous and crystalline states. For this aim, a sample of bulk efavirenz was heated to 140 °C to ensure melting. Afterwards it was cooled down to -50 °C, at a rate of 10 °C/min, with data being recorded at 5 frequencies (10^2, 10^3, 10^4, 10^5

and 10^6 Hz). Next, it was heated to 80 °C, the crystallization temperature, at 10 °C/min and data was recorded in the 5 frequencies previously mentioned. Finally, isothermal dielectric spectra were gathered at 80 °C, where all parameters were measured every 90 seconds, in the frequency range of 10^{-1} to 10^6 Hz.

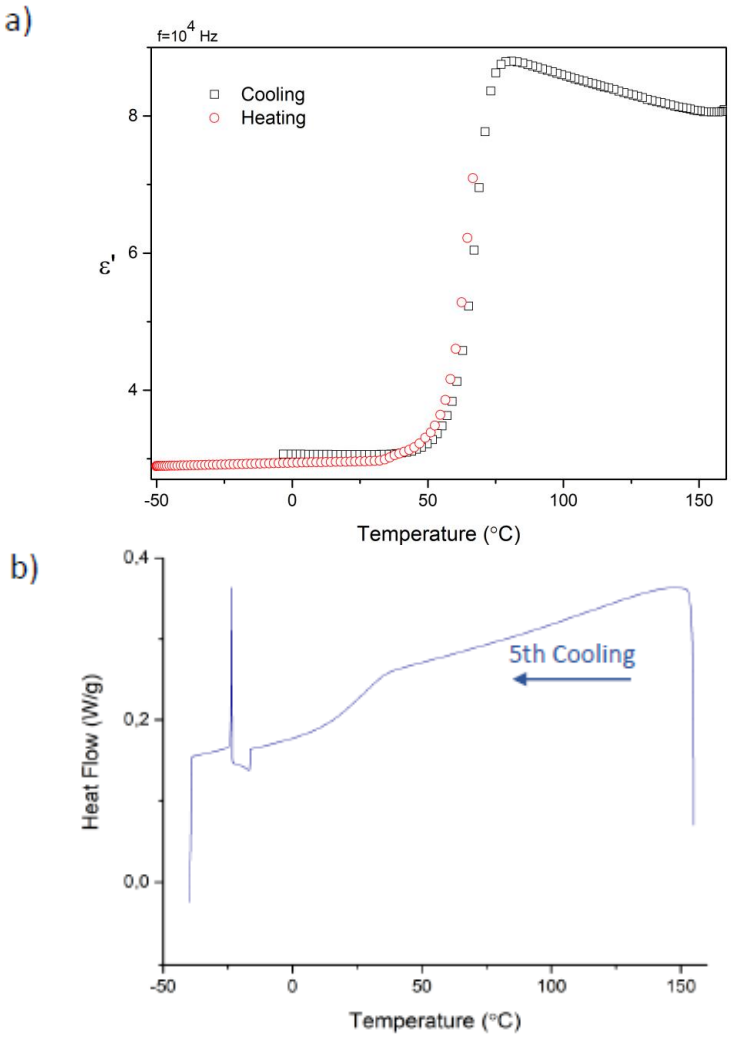

Figure 3.20: a)Isochronal representation of ε' at the frequency of 10^4 Hz: the black symbols (square) correspond to the cooling of the sample at 10 °C/min and red symbols (circle) correspond to the subsequent cooling at 10 °C/min; b)Thermogram of bulk efavirenz during cooling at 10 °C/min, from 155 °C to -40 °C (from figure 3.14).

Figure 3.20 illustrates the cooling of the sample from 160 °C to -44 °C at 10 °C/min (run 1), in which the real permittivity was tracked at the frequency of 10^4 Hz. Crystallization does not occur as seen by the lack of a discontinuity. As the sample is cooled, three is a decrease in the real permittivity close to 65 °C. This decrease is observed at

different temperatures when the frequency is changed, indicating that the underlying phenomenon has a kinetic nature. Then, the crystallization can not be ascribed, and given the proximity to the Tg values obtained by DSC, it is easy to associate to the vitrification of the sample. There is also a small discontinuity at ≈ 3 °C. In the subsequent heating (run 2) from -50 °C to 66 °C also at 10 °C/min, given that the values of both runs are superimposed, we can conclude that up until 66 °C no crystallization occured.

In order to study the crystalline state, the variation of permittivity during the crystallization temperature was monitored (see figure 3.21). Overall, with time there is an asynchronous decrease of the permittivity value.

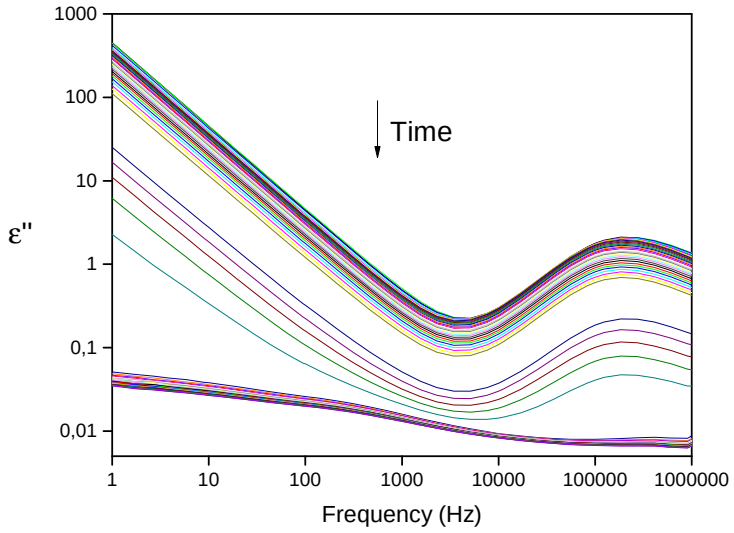

Figure 3.21: Permittivity spectra of efavirenz taken at 80 °C. The spectra were collected every 90 s for the first 3510 s, and every 180 s for another 4680 s.

To allow a more detailed analysis of the dielectric response, the model function introduced by Havriliak-Negami (HN) [63] was fitted to the experimental data. This function is an empirical modification of the Debye relaxation and accounts for the broadness and asymmetry of the dielectric dispersion curve.

$$\varepsilon^*(f) = \varepsilon_\infty + \sum_j \frac{\Delta\varepsilon_j}{[1 + (i\omega\tau_{HN})^{\alpha_{HN}j}]^{\beta_{HN}j}} \tag{3.2}$$

Where j is the index over which the relaxation processes are summed; $\Delta\varepsilon$ is the dielectric strength; τ_{HN} is the characteristic HN relaxation time; and α_{HN} and β_{HN} are fractional parameters ($0 < \alpha_{HN} \leq 1$ and $0 < \alpha_{HN}\beta_{HN} \leq 1$) describing, respectively, the symmetric and asymmetric broadening of the complex dielectric function.

An example of the fitting procedure is presented in figure 3.22, for t=180s and t=8010s. At the initial moments, the spectra is well described by one HN function located at high frequencies and the dc contribution (figure 3.22 a)). As crystallization evolves,

this peak loses intensity while maintaining the frequency position. A sudden change in the spectra profile is observed around 3400s, including a shift to higher frequencies and an abrupt decrease of $\Delta\varepsilon$ of the α-process. From this moment it was necessary to use two additional HN relaxations (without conductivity) to describe the overall spectra (figure 3.22 b)). The process located around 2 X 10^2 Hz will be named α' and may be associated to the amorphous fraction entrapped in the crystal structure formed [64].

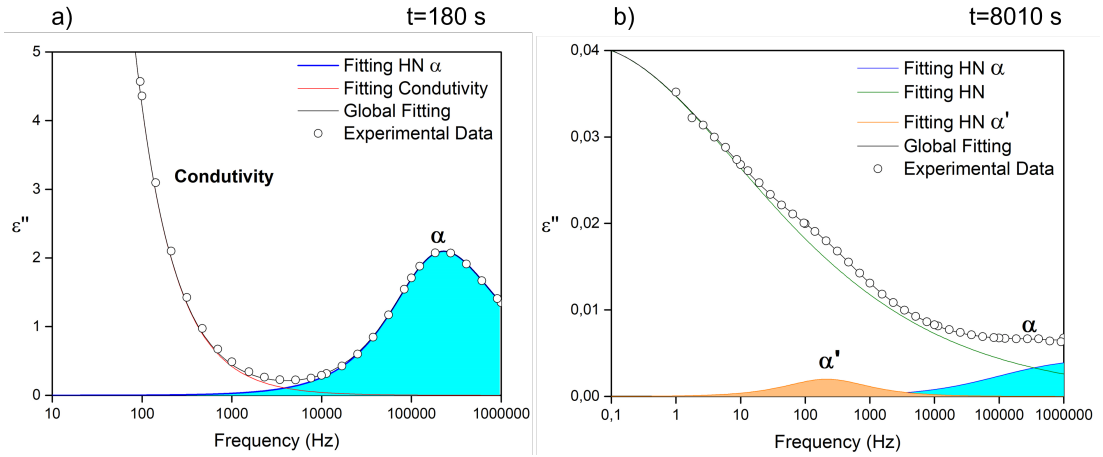

Figure 3.22: Dielectric spectrum collected for crystallization (80 °C) at: a) 180 s; b) 8010 s. Individual fitting functions are represented by colored lines, the overall fitting by a black line and experimental data by open circles.

The time dependence of the dielectric strength of the processes that become progressively immobilized during the evolving of crystallization, $\Delta\varepsilon_\alpha$, is shown in figure 3.23 a). The degree of crystallization, χ_{cr}, can be estimated from that time dependence using the following relation:

$$\chi_{cr} = 1 - \frac{\Delta\varepsilon_\alpha(t)}{\Delta\varepsilon_\alpha(t=0)} \tag{3.3}$$

where $\Delta\varepsilon_\alpha$(t=0) represents the intensity of the α-relaxation observed for the crystallization time t=0 and $\Delta\varepsilon_\alpha$(t) the intensity at any instant. The resulting data is plotted in figure 3.23 b) and can be used to extract kinetic information of the crystallization. In accordance with the Avrami model [65], the degree of crystallization can be described by equation 3.10, that can be modified taking into account an induction time at the beginning of the crystallization as equation 3.5.

$$\chi_{cr} = 1 - \exp(-kt^n) \tag{3.4}$$

$$\chi_{cr} = 1 - \exp\left(-\left(\frac{t-t_0}{\tau_{CR}}\right)^n\right) \tag{3.5}$$

k is a temperature-dependent rate constant and n is the Avrami parameter that can take values between 1 and 7 depending on nucleation type and crystal growth mechanism.

τ_{CR} is obtainable from the Avrami parameters by the relationship $\tau_{CR}=k^{-1/n}$. The fitting parameters obtained are: t_0=0 s, τ_{CR}=2384±26 s and n=2.4±0.1. The low Avrami exponent could be interpreted as a crystal growth of low dimensionality [66].

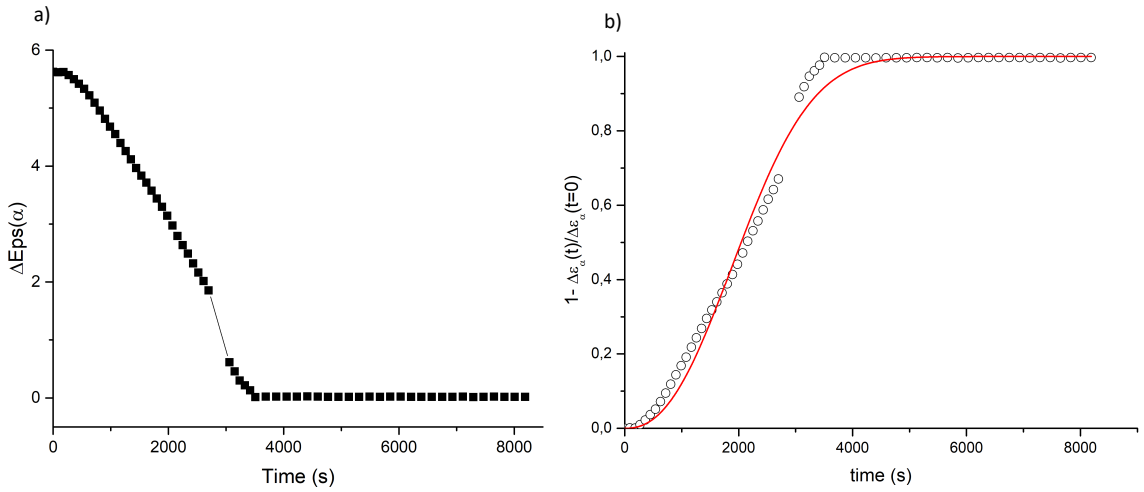

Figure 3.23: Time evolution of: a) dielectric strength, $\delta\varepsilon_\alpha(t)$, for the amorphous fraction; b) crystallinity degree estimated following equation 3.11. Cold crystallization monitored at 80 °C and followed during 8010 s. Solid line represents the fit with equation 3.10

3.7.2 Unloaded and Loaded Silica

Dielectric studies were carried to access the molecular mobility of efavirenz confined by the silica. The real, ε', and imaginary, ε", parts of the complex dielectric permittivity of unloaded silica was plotted in function of temperature at a fixed frequency. These isochronal plots are shown in figure 3.24, for the frequency of 1 kHz.

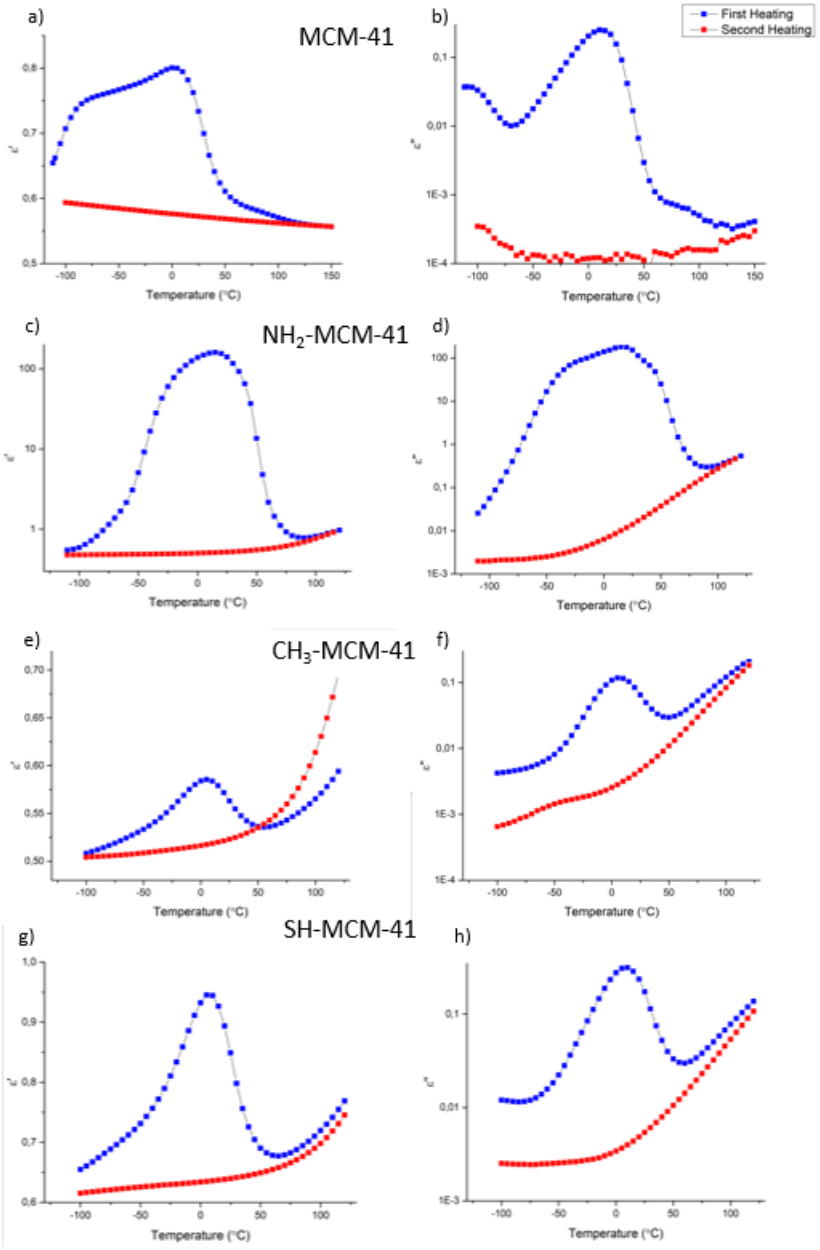

Figure 3.24: Isochronal representation of ε' (left) and ε'' (right), at the frequency 1 kHz for unloaded silica: (a, b) MCM-41; (c, d) NH_2-MCM-41; (e, f) CH_3-MCM-41 and (g, h) SH-MCM-41. Blue and red data correspond to first and second heating respectively.

In all four silica there is a similar pattern, where in the first heating there is a high dielectric response that decreases in the second heating. This response comes from the water present in the samples, since the water molecules have a high dipolar moment. As the first heating occurs and the temperature increases, the water adsorved in the silica starts to evaporate therefore leading to the decrease of the signal, at around 50 °C. For the bare silica the, the final value of ε' is lower than the initial, evidence of the removal of water from the sample. In MCM-41, there are two peaks around -108 °C and 11 °. In NH_2-MCM-41, two peaks are also present although far less defined, at -35 °C and 17 °C.

For the remaining two samples, CH_3-MCM-41 and SH-MCM-41, there is only one peak located around 5 °C. A comparable water process to the one observed at around -108 °C in MCM-41 is reported in [67] below -80 °C. For the CH_3-MCM-41 and SH-MCM-41, there is also an increase in the dielectric response at higher temperatures. For this reason, it appears that the water present in these samples is not totally drawn out and even continues adsorved at temperatures higher than 100 °C. These processes can also be identified in a ε"(f) spectrum (see figure A.2). The similar processes in CH_3-MCM-41 and SH-MCM-41 both shift to higher frequencies as the temperature reaches positive values. For NH_2-MCM-41, this process dislocates more swiftly across the frequency range, being already present at high frequencies at -40 °C. Lastly, two processes are clear in the MCM-41 spectrum, with much lower intensities than the functionalized samples.

The data of the unloaded NH_2-MCM-41 silica was further analyzed. Figure 3.25 shows the dielectric loss spectra taken isothermally using the permittivity and the dielectric modulus (M") representation.

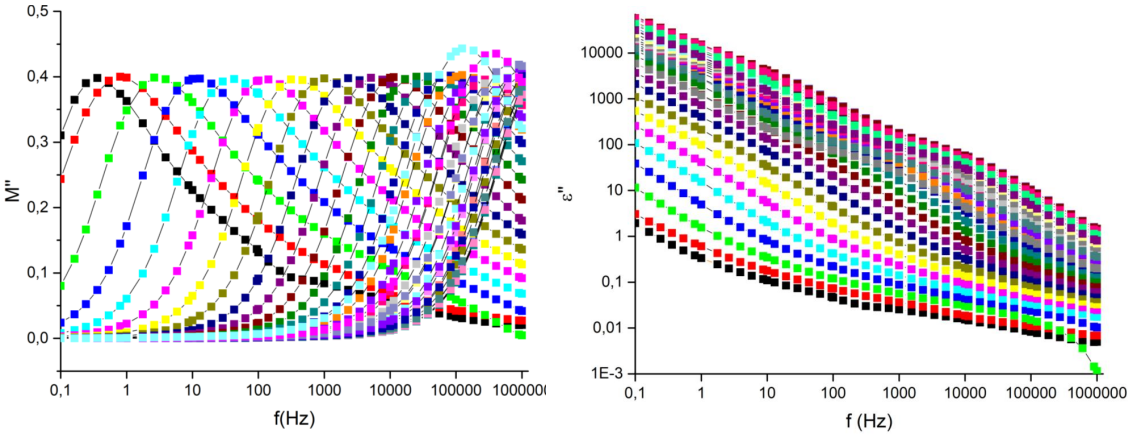

Figure 3.25: Isothermal M" and ε" spectra of unloaded NH_2-MCM-41 matrix for temperatures from -110 to 50 °C every 5 degrees.

Overall, with the increase of the temperature there is a shift of the ε" peaks to higher frequencies, even clearer in the modulus representation. This shift happens due to the higher mobility derived from the higher temperature and inverse relationship between time and frequency.

The dielectric data was also analyzed via the complex electrical modulus (M*). The imaginary part of M*, M*(ω) = M'(ω) + iM"(ω) was simulated by sum of individual HN-like functions [68].

$$M^*(\omega) = M_\infty + \frac{\Delta M}{(1 + (-i(\omega\tau_{HN-M})^{-1})^{\alpha_{HN}})^{\beta_{HN}}} \tag{3.6}$$

The peaks observed in the previous isochronal representation of M" where analyzed. Both heating series were taken into account for the analysis, to better understand the processes

occurring in these matrices. Figure 3.26 represents M" vs frequency at 95 °C for both series.

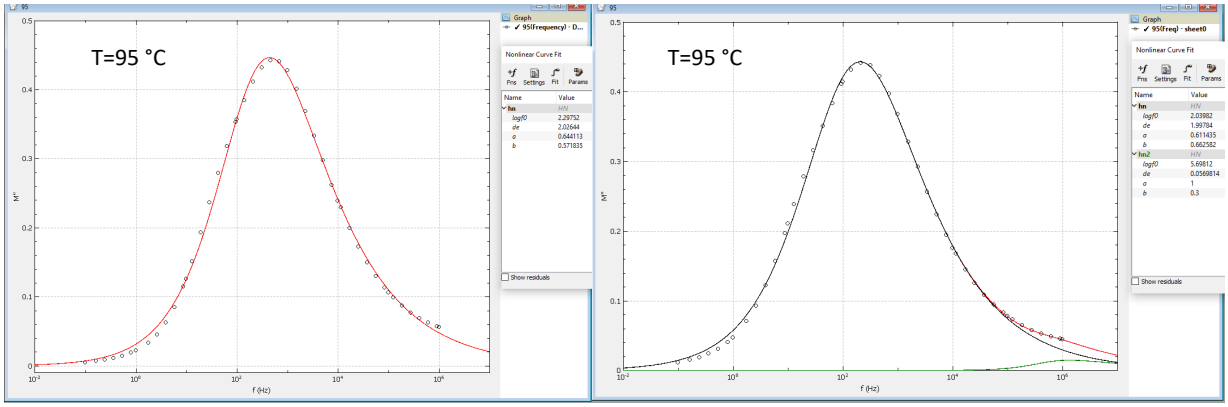

Figure 3.26: Dielectric spectrum taken at 95 °C for: a) the first serie and b) the second serie of NH_2-MCM-41. The colored lines represent the fitting of data.

From this fitting the most important parameter is the relaxation time, τ_{HN}, that is then converted to τ_{max} in accordance with the following equation:

$$\tau_{max} = \tau_{HN}\left[\sin\left(\frac{\alpha_{HN}\pi}{2+2\beta_{HN}}\right)\right]^{-\frac{1}{\alpha_{HN}}}\left[\sin\left(\frac{\alpha_{HN}\beta_{HN}\pi}{2+2\beta_{HN}}\right)\right]^{-\frac{1}{\alpha_{HN}}} \tag{3.7}$$

Following this, the temperature dependence of relaxation time is represented in a relaxation map, -log(τ_{max} vs. 1000/T), plotted in figure 3.27. In this plot, data corresponding to MCM-41 was taken from [69] and data of APTES functionalized mesoporous silica nanoparticle (MSN_APTES) from [70], and included in the figure. This extra data allows for the comparison of NH_2-MCM-41 with a non-functionalized MCM-41 (MCM-41_2) and another silica with the aminopropyl functional group. Additionaly, all of these silica have a similar pore size.

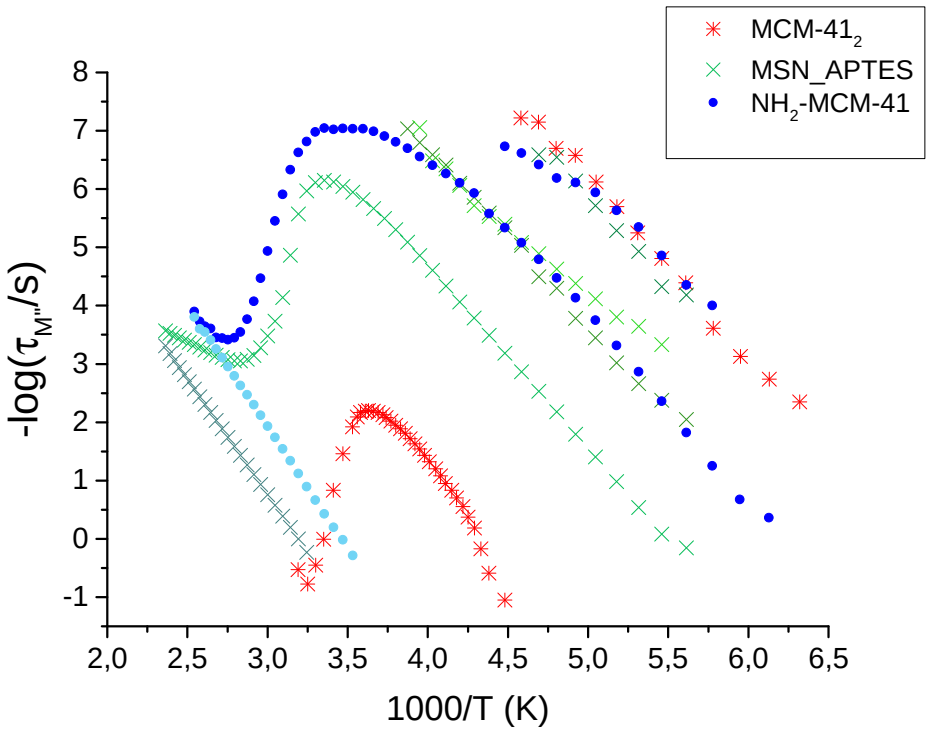

Figure 3.27: Relaxation map of all processes detected in unloaded matrices NH_2-MCM-41, MCM-41$_2$ [69] and MSN_APTES [70] (fitting in M"(f)).

NH_2-MCM-41 presents a low T water process (blue circles, designated as process I), also visible in the other two samples, which can be attributed to the reorientation of water molecules in ice-like structures [71]. This process follows a linear temperature dependence, described by an Arrhenius equation:

$$\tau(T) = \tau\infty \exp(Ea/RT) \tag{3.8}$$

The estimated activation energy of the previous process for NH_2-MCM-41 is 40 kJ/mol and τ_∞ is 4.4 x 10^{-17} seconds (see table 3.8). It becomes clear that the chemical modification of the particles influences the activation energy, given the significant decrease in energy when compared to the other two samples. The interaction of NH_2-MCM-41 with water causes a decrease of the activation energy relatively to bulk ice, with reported values of about 46-49 kJ/mol [72]. Given this, it is possible that there is a weaker interaction between the water clusters and the aminopropyl groups present in the inner pore surface.

Table 3.8: Activation parameters for unloaded silicas. The relaxation times of process I and II were fitted with equation 3.8.

	Process I		Process II		
	E_a (kJ/mol)	τ_∞ (s)	E_a (kJ/mol)	τ_∞ (s)	T_{max} (°C)
NH_2-MCM-41	40	4.4×10^{-17}	58	1.5×10^{-19}	25.0
MSN_APTES	55	4.7×10^{-21}	60	6.3×10^{-18}	21.8
MCM-41_2	58	6.2×10^{-22}	68	4.0×10^{-16}	2.3

The second process (process II) has a distinctive temperature dependence, where from -110 to 15 °C the relaxation times increase with higher temperatures, and up to 100 °C these dynamics slow down. The variation gives rise to a saddle-like temperature dependence, as seen in other porous silica materials [73]. This process not only presents itself in a wider temperature range, in comparison to MCM-41_2, but is also shifted from MSN_APTES by ≈ 3 °C.

This particular shape derives from the increased mobility of loosely bound water as temperature increases, progressing as a thermally activated process in the low-T branch. Meanwhile, in the high-T branch, there are two mechanisms occurring. There is removal of nearly free water by the nitrogen flow in the sample cell and temperature increase. On the other hand, the reorientational motions of the remaining water molecules, more strongly bound to the pore surface, are slowing down. In the low-T branch, the temperature dependence of the relaxation times obey the Arrhenius equation 3.8, allowing fo the estimation of activation energy and pre-exponential factor τ_∞ (see table 3.8.) The higher temperature value of the kink point of the saddle process for NH_2-MCM-41 is a good indicator of its higher ability to retain water.

In the second series of NH_2-MCM-41 (light blue circles), there is yet another process only seen from 10 °C, also with a linear temperature dependence, derived from the water still present in the sample even after the first heating cycle. From these results, it becomes clear that introducing aminopropyl groups on the pore surface increases the water afinity of theses matrices.

Posterior to the efavirenz incorporation, the dielectric response of the composites was monitored an seen in the isochronal representation displayed at 1 KHz in figure 3.28 of the real, ε' (left), and imaginary , ε'', parts of the complex permittivity for the first (hydrated; filled symbols) and second (dehydrated; open symbols) series. Data for bulk EFZ is also included in figure 3.28 (black symbols). By comparing both sets of data, it is possible to attribute the dielectric response between 40 and 90 °C to efavirenz. In the low T zone, the previously characterized water processes are also visible. After dehydration, these processes vanish in all the samples.

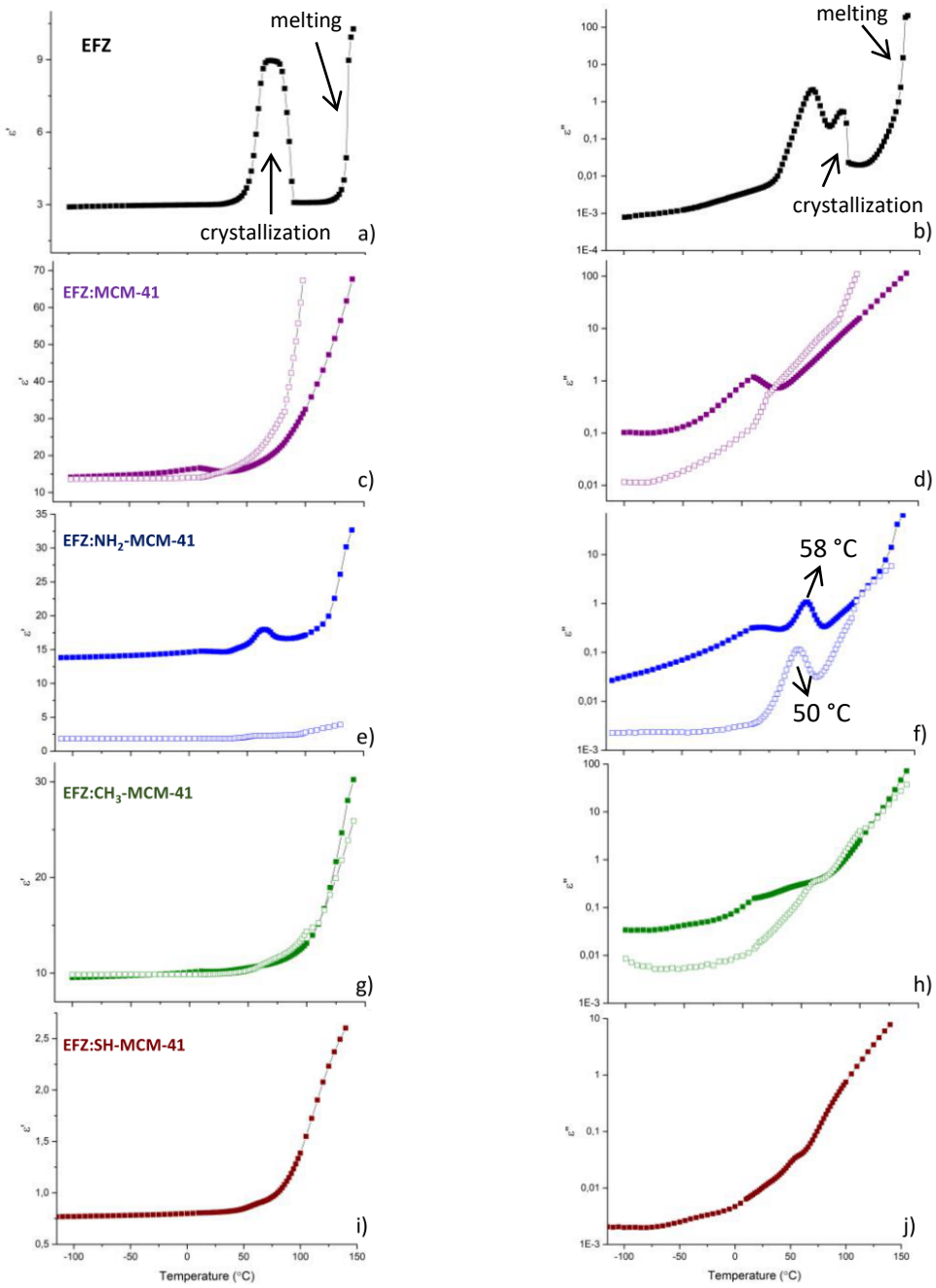

Figure 3.28: Isothermal representation of ε' (left) and ε'' (right) vs. temperature at f=1 kHz for (a,b) efavirenz, (c,d) EFZ:MCM-41, (e,f) EFZ:NH_2-MCM-41, (g,h) EFZ:CH_3-MCM-41 and (i,j) EFZ:SH-MCM-41. The filled and open symbols are for hydrated and dried data, respectively.

The previous calorimetric analysis demonstrated that efavirenz undergoes cold crystallization around 90 °C (table 3.4) and melting close to 136 °C (figure 3.12). This is can be observed in DRS as a sharp decrease, crystallization, and later increase (melting) in both parts of complex permittivity. In all composites, the signals associated with efavirenz can

be observed, although they are much clearer in EFZ:MCM-41 (figure 3.28 d)) and specially EFZ:NH_2-MCM-41 (figure 3.28 f)). For EFZ:NH_2-MCM-41 no crystallization is observed and there is a minor discontinuity possibly from the melting of residual efavirenz outside the pores, coherent with DSC results (figure 3.19). The existance of this small discontinuity means that the majority of EFZ is in the amorphous state, with a crystalline fraction still present. In the first series (filled blue symbols), there is an additional less intense relaxation at around 15 °C, whose origin cannot be attributed exclusively to water. In the subsequent section, the dielectric response of efavirenz incorporated in NH_2-MCM-41 will be analyzed further. This composite, EFZ:NH_2-MCM-41, was chosen due to the clear profile of the drug in the isothermal spectra. For the first series (hydrated), the fitting analysis was carried out for data acquired between 38 and 140 °C, and for the second series (dried) between 16 and 140 °C. Furthermore, this data was analyzed with a sum of HN functions (equation 3.8). A reperesentation of the fitting curves for the first series of EFZ:NH_2-MCM-41 and data of bulk efavirenz are included in figure 3.29.

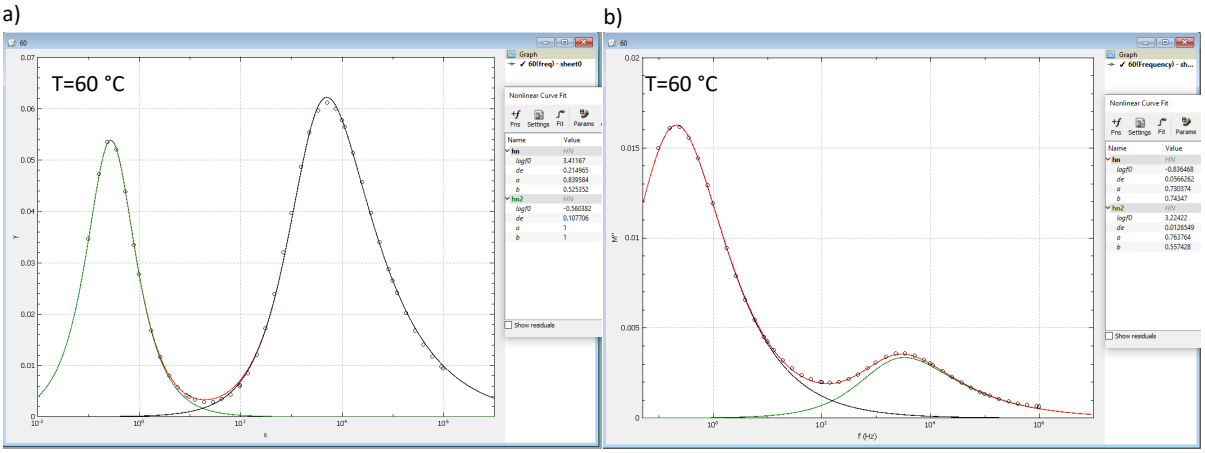

Figure 3.29: Dielectric spectrum taken at 60 °C for: a) bulk efavirenz and b) the first series of EFZ:NH_2-MCM-41. The colored lines represent the fitting of data.

The temperature dependence of the relaxation times for the detected processes are represented in figure 3.30 (hydrated-closed symbols; dried-open symbols). The processes pertaining to bulk efavirenz are also represented as red symbols.

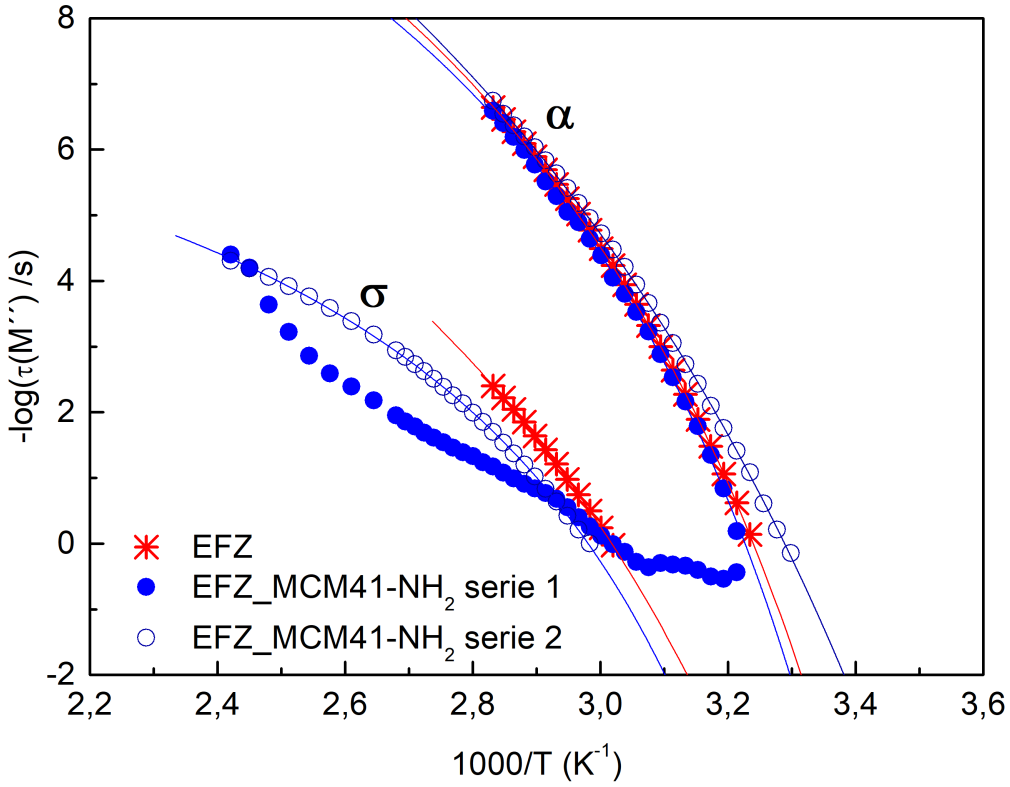

Figure 3.30: Relaxation map of all processes detected in EFZ:NH_2-MCM-41 (blue symbols) and bulk efavirenz (red symbols). Filled and open symbols correspond to hydrated and dried data, respectively. The solid lines are fitting functions with VFTH estimated for each process.

The relaxation times of the two processes present in the relaxation map exhibit a non-linear temperature dependence of relaxation time, which is described by the Vogel/Fulcher/Tammann/Hesse (VFTH) equation [74]:

$$\tau(T) = \tau_{\infty} \exp\left(\frac{B}{T - T_0}\right) \tag{3.9}$$

where τ_{∞} is the relaxation time value in the high temperature limit, B is an empirical parameter characteristic of the material accounting for linearity deviation and T_0 is the Vogel temperature that can be related to the glass transition temperature of an ideal glass [75]. The activation energy, E_a in this scenario is obtained by the following equation:

$$E_a = R\frac{\partial \ln \tau}{\partial (1/T)} = \frac{R.B}{(1 - T_0/T)^2} \tag{3.10}$$

In the low temperature side of the relaxation map, a relaxation process is detected for bulk efavirenz and both series of the composite. This is the α-process of efavirenz, originating from the dynamic glass transition [76]. From this, the dielectric glass transition

temperature was estimated by extrapolating the fitted curve (red) at τ=100s. This value has significance, and originates from the Maxwell relationship of viscosity η and the shear modulus G, conveyed by η=Gτ (assuming viscosity≈10^{12} Pa and G≈10^{10} Pa for a solid material) [77]. The extrapolated value for bulk efavirenz at τ=100s is T_g=28.5 °C, in good agreement with the T_g=30.7 °C reported in literature [60]. Although this value is lower than that obtained by DSC, T_g=33.0 °C, the difference can be explained given that two different techniques were used. The remaining parameters for this process are displayed in table 3.9.

Table 3.9: Estimated parameters of VFTH fit for the α-process in all samples.

Parameters	Bulk EFZ	EFZ:NH_2-MCM-41 (Serie 1)	EFZ:NH_2-MCM-41 (Serie 2)
E_a (kJ/mol)	560	604	442
$T_{g,DRS}$ (°C)	28.5	30.1	22.5
τ_∞ (s)	7.22 X 10^{-17}	1.04 X 10^{-15}	2.01 X 10^{-17}
B (K)	2359.5	1937.9	3731.7
T_0 (K)	245.2	253.7	217.3

As the temperature decreases, the relaxation times for confined efavirenz deviate from bulk EFZ. For the hydrated series this deviation is small, but for the dried series is more significant. As the temperature decreases, the behavior of confined efavirenz deviates from the behavior of the bulk drug. This deviation signifies less restriction of confined efavirenz and is apparent in the glass transition temperature, of T_g=22.5 °C, ≈ 8 °C lower than bulk EFZ and lower activation energy. The secondσ-process The σ-process originates closely to the α-process, and in the hydrated series (filled blue symbols) progresses in a non-uniform matter. It is only at 144 °C that the two series overlap. This behavior occurs due two factors: as the temperature increases, water evaporates from the sample. On the other hand, adsorbed water in the innermost layer of the pores becomes more strongly adsorbed. Given that both the α and σ-processes can be described by a VFTH function, it is possible they are correlated.

Another parameter that can be obtained is the fragility m index defined as:

$$m = \frac{\partial \log \tau}{\partial (T_g/T)_{T=T_g}} = \frac{E_a(T_g)}{\ln 10 R T_g} \tag{3.11}$$

where the T_g value is the one estimated by extrapolation at 100s. This index reflects the stability of a structure to thermal degradation [64]. The hydrated and dried series have a fragility index of 104 and 78, respectively. Given this, this composite has a lower fragility when dry. It is possible to conclude that for EFZ:NH_2-MCM-41, efavirenz develops a greater mobility when the sample undergoes drying, evidence of the significant role water has in these mechanisms.

3.8 Controled Release Studies

The in vitro release profiles of the composites and native efavirenz are shown in figure 3.31.

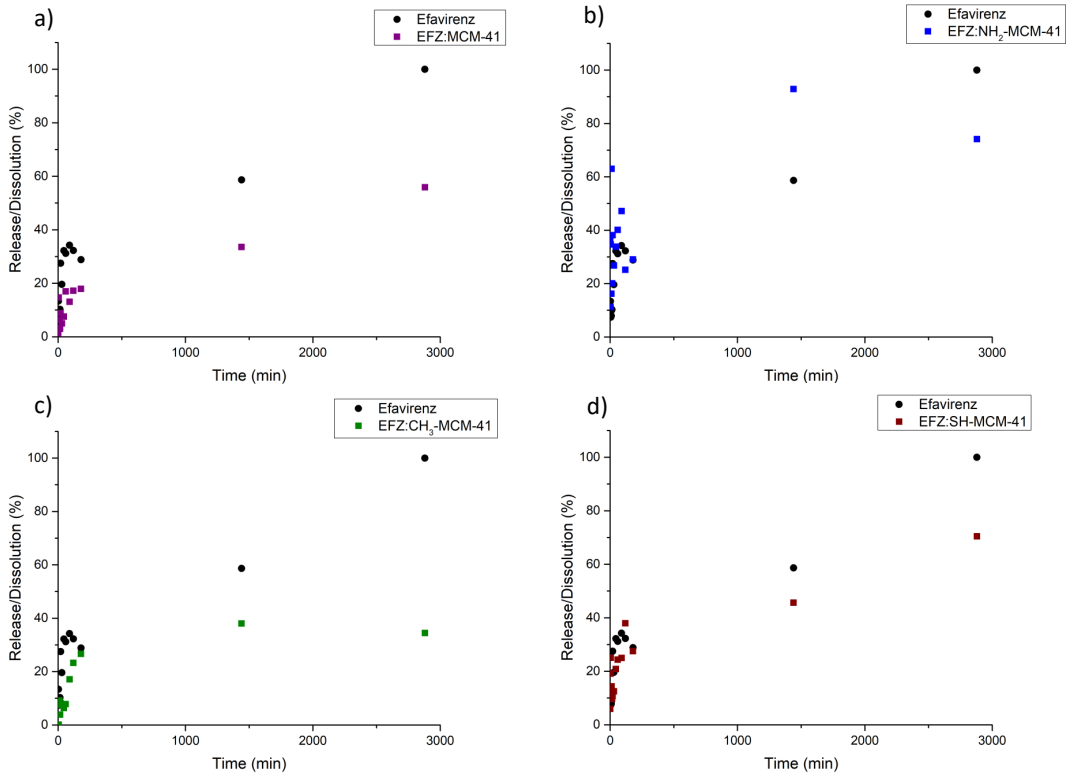

Figure 3.31: In vitro release profiles of native efavirenz and: a) EFZ:MCM-41; b)EFZ:NH_2-MCM-41; c) EFZ:CH_3-MCM-41 and d) EFZ:SH-MCM-41.

The release profiles of all the composites are similar between them. There is an initial burst release of the drug of approximately 10-20 % during the first 20 minutes. Afterwards, there is a continuous release that never reaches 100 %, similar to what is reported in literature [9]. Of all the composites, EFZ:CH_3-MCM-41 has the slowest release rate with only 34 % being released after 48 hours. This is likely due to the smaller pore size.

When comparing EFZ:MCM-41 to the other samples, two distinct effects were observed: i) for EFZ:NH_2-MCM-41 the release rate increases, likely due to the drug molecules being weakly entrapped inside the mesopores. ii) for EFZ:CH_3-MCM-41 and EFZ:SH-MCM-41 the release rate decreases, specially for EFZ:CH_3-MCM-41. This is in accordance with the smaller pore size of these matrices.

The results indicate that the release profiles are dictated by several factors such as the structure of the mesoporous material, such as the pore size, and the organic groups present on the surface of mesoporous structure.

Upon looking closely at the first 100 minutes of the release profiles (see figure), the initial release of efz is more apparent. After 20 minutes, for EFZ:CH_3-MCM-41 and EFZ:SH-MCM-41, there is a plateau like behavior where the percentage of efavirenz being released does not alter significantly until further on the release study. For the other two samples, the release continually increases up to the 48 hours. Even though the presence of EFZ outside the pores was detected, the matrices still exert influence on the initial release of drug.

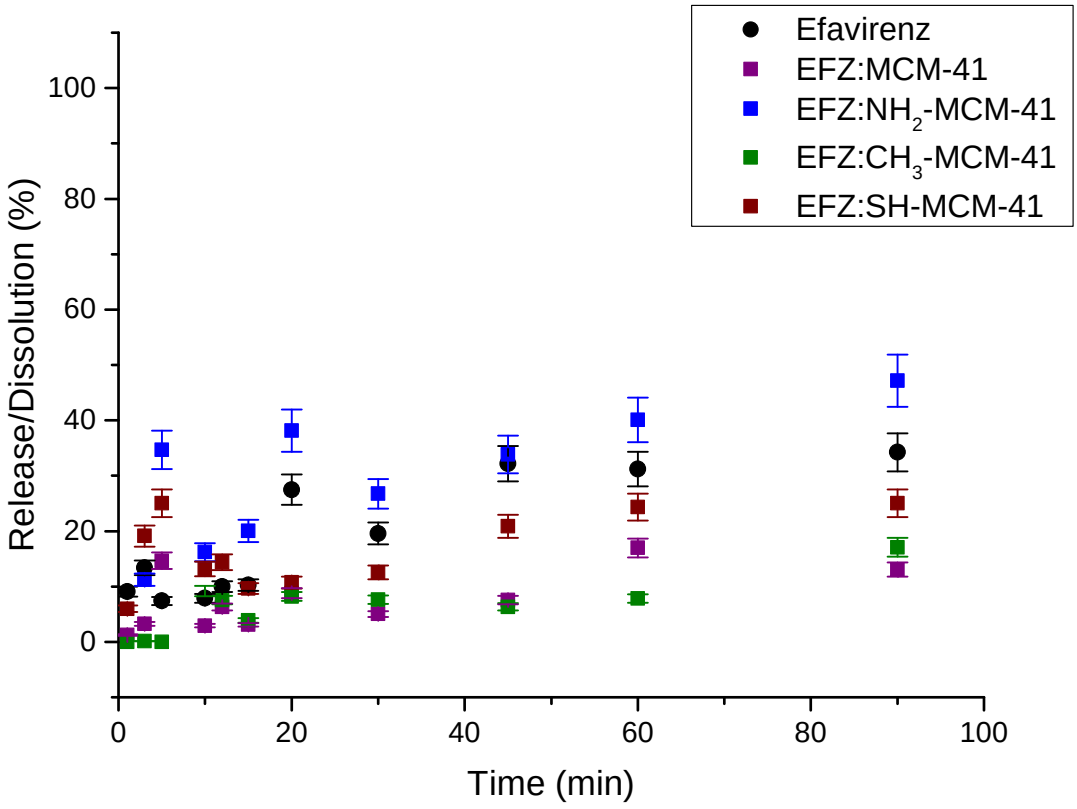

Figure 3.32: In vitro release profiles of native efavirenz and: a) EFZ:MCM-41; b)EFZ:NH_2-MCM-41; c) EFZ:CH_3-MCM-41 and d) EFZ:SH-MCM-41. Zoom on the first 100 minutes.

The release profile of these matrices can be rationalized by looking at the pka values of the functional groups present on the pore surface. These are silanol, aminopropyl, methyl and mercaptopropyl, with pka values of 4.5-8.5 [78], 10.8 [79], 50 [80] and 10.2[78]. Given the lack of reactivity of the methyl group, it only contributes to passivating the inner pore surface. Efavirenz has a pka of 10.2 [81] and the release experiments were conducted at pH=7.4. At this pH, these functional groups (with the exception of the methyl) and the drug are protonated in solution. As the difference of the pka and pH value increases, the charge is also greater and there is increased repulsion between the organic groups and the

drug, as follows: -$(CH_2)_3$-NH_2>-$(CH_2)_3$-SH>-Si-OH>-CH_3. This order coincides with the percentage of drug release in the composites, with EFZ:NH_2-MCM-41 having the most electrostatic repulsions with efavirenz and therefore releasing the highest amount of all samples.

Another type of release study was done for EFZ:MCM-41, EFZ:NH_2-MCM-41 and EFZ:CH_3-MCM-41 to further analyze the release profile. The solution for drug release was also phosphate buffer, at pH=7.4, and the base line was done with a quartz cuvette. Drug release was monitored for about 10 hours by Uv-Vis spectroscopy. For this a dialysis tube with a cellulose membrane separates the top and bottom chamber of a quartz corvette. The sample in 1 µL of buffer was added to the top chamber and the bottom chamber filled with 3mL of phosphate buffer and kept under stirring at 200 rpm. For the first 238 minutes, spectra was taken every 2 minutes and for the remaining time every 4 minutes (200-700 nm) at an acquisition rate of 400nm/min. To analyze the release profile, absorvance at 240 nm was represented in function of time (figure 3.33).

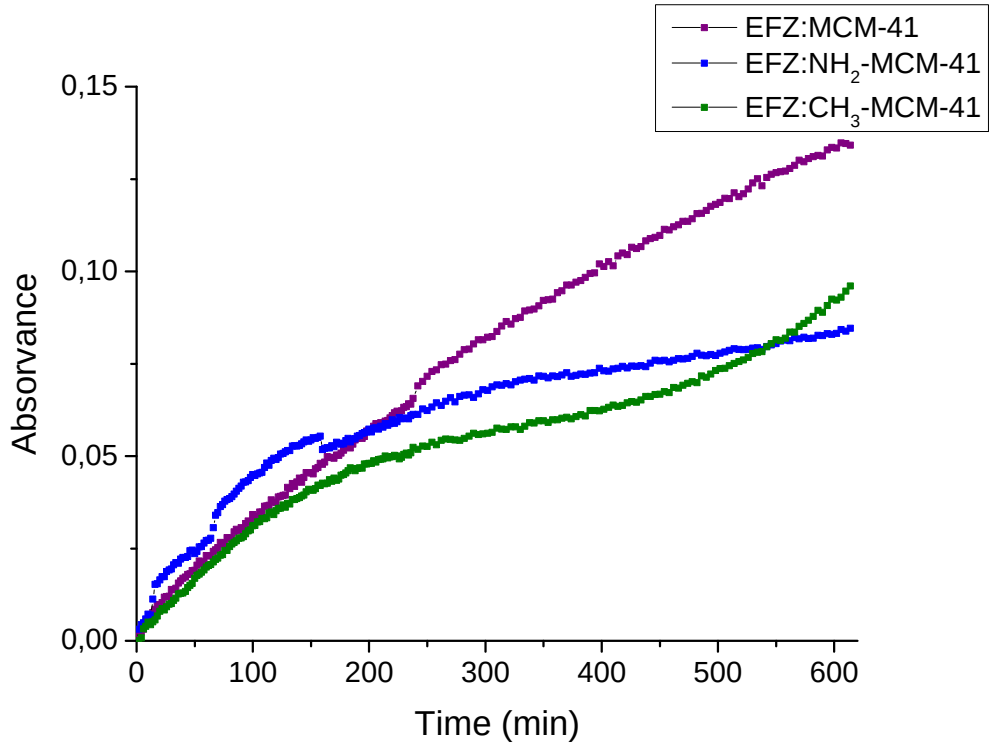

Figure 3.33: In vitro release profiles of EFZ:MCM-41 (purple), EFZ:NH_2-MCM-41 (blue) and EFZ:CH_3-MCM-41 (green).

For all the samples there is a gradual increase of EFZ release and no initial faster dissolution is observed. Since a similar amount of all composites was used for the release study, it is possible to compare the absorvance values, even if qualitatively. During the first 158 minutes, the release follows a similar pattern to the previous release study: EFZ:NH_2-MCM-41 releases the highest quantity of efavirenz, followed by EFZ:MCM-41 and then EFZ:CH_3-MCM-41. After, this order starts to shift, to where at the end of the study

EFZ:MCM-41 has released the most drug, with EFZ:CH_3-MCM-41 after. Even though this is not what was observed in the previous release study, comparisons between the two cannot be made since not only are there different conditions but also the release profiles were followed for different total times and time intervals. One additional observance can be made in regards to the shape of the release curves. EFZ:MCM-41 appears to follow an almost linear release, EFZ:NH_2-MCM-41 almost plateus after 300 minutes although there could be another increase of the values towards the final minutes (additional experimental data would be needed to confirm this hypothesis). Finally, EFZ:CH_3-MCM-41 has an inverted S-like shape. All of this further highlights how differently the matrices interact with efavirenz.

4

Conclusion

This work aimed to stabilize the amorphous state of efavirenz, to increase aqueous solubility. For this, the drug was incorporated into mesoporous silica, both bare and with surface modifications, and the drug release profile was analyzed.

Mesoporous silica particles (MCM-41) with regular pores of 3.4 nm were synthesized. The pore surface of these particles was modified with three organosilanes containing the following functional groups: aminopropyl (NH_2-MCM-41), methyl (CH_3-MCM-41) and mercaptoporpyl (SH-MCM-41).

The sucess of the modification was confirmed by nitrogen adsorption-desorption analysis, elemental analysis, ATR-FTIR and ^{1}H NMR. The pore size obtained for the functionalized silica varied from 3.07-2.69 nm. In addition, the particle size also varied drastically, from MCM-41 with 591 nm to SH-MCM-41 with 110 nm. The presence of the functional groups was observed in ATR-FTIR and ^{1}H NMR spectra. Elemental analysis helped to elucidate the presence of surfactant on these samples and even obtain a percentage of the compound present in the samples (7-10%). Afterwards, efavirenz was loaded onto the four different silicas, originating four composites: EFZ:MCM-41, EFZ:NH_2-MCM-41, EFZ:CH_3-MCM-41 and EFZ:SH-MCM-41. FTIR spectra clearly show that efavirenz was adsorbed in the matrices and interacting with the pore surface.

Differencial scanning calorimetry (DSC) and dielectric relaxation spectroscopy (DRS) allowed the gathering of information of the physical state of confined EFZ. DSC showed that amorphous efavirenz was successfully stabilized, given the absence of recrystallization peaks and presence of the glass transition step, at $T_g \approx 25$ °C. These glass transitions were much wider than that of bulk EFZ. Furthermore, in EFZ:NH_2-MCM-41 and EFZ:CH_3-MCM-41 a melting peak was present, at T_m=137 °C, from EFZ present outside the pores.

DRS allowed for the investigation of the molecular mobility of efavirez. In all the composites, no significant sign of melting is observed, once again confirming that EFZ is stabilized in its amorphous state. Additionally, for EFZ:NH_2-MCM-41 the α-process (associated with glass transition) is very clear. A glass transition temperature was estimated from dielectric data and is congruent with the calorimetric T_g. The effect of water was

also seen, since in the dried series, the dielectric T_g and activation energy values were much lower than that of bulk EFZ suggesting a higher molecular mobility for the drug when adsorbed water in the sample is removed.

The release of EFZ from the composites was followed by Uv-Vis spectroscopy. Here, EFZ:NH_2-MCM-41 had the fastest release over the course of 48 hours, although 100 % was never achieved. This fact indicates all the composites are capable of controlling the release process for even longer periods of time.

In conclusion, by functionalization of MCM-41 pores it is possible to stabilize the amorphous state of efavirenz and tune the drug release profiles.

5

Future Works

In further studies, it would be of interest to perform nitrogen absorption-desorption studies of the composites. Quantification of the organic groups in the pore surface by ^{1}H NMR would contribute for the improvement of the synthesis protocol. A more detailed study of dielectric data of the remaining composites, similarly to EFZ:NH_2-MCM-41, would help to further comprehend the molecular mobility of confined efavirenz. Finally, kinetics models should be applied to the drug release profiles.

Bibliography

[1] J. M. Lourenço. *The NOVAthesis LaTeX Template User's Manual*. NOVA University Lisbon. 2021. URL: https://github.com/joaomlourenco/novathesis/raw/master/template.pdf (cit. on p. ii).

[2] H. D. Williams et al. "Strategies to address low drug solubility in discovery and development". In: *Pharmacological reviews* 65.1 (2013), pp. 315–499. DOI: https://doi.org/10.1124/pr.112.005660 (cit. on p. 1).

[3] T. Das, C. H. Mehta, and U. Y. Nayak. "Multiple approaches for achieving drug solubility: an in silico perspective". In: *Drug discovery today* 25.7 (2020), pp. 1206–1212. DOI: https://doi.org/10.1016/j.drudis.2020.04.016 (cit. on p. 1).

[4] S. May and A. Fahr. "Self-Assembled Delivery Vehicles for Poorly Water-Soluble Drugs: Basic Theoretical Considerations and Modeling Concepts". In: *Drug Delivery Strategies for Poorly Water-Soluble Drugs* (2013), pp. 1–35. DOI: https://doi.org/10.1002/9781118444726.ch1 (cit. on p. 1).

[5] M. Rodriguez-Aller et al. "Strategies for formulating and delivering poorly water-soluble drugs". In: *Journal of Drug Delivery Science and Technology* 30 (2015), pp. 342–351. DOI: https://doi.org/10.1016/j.jddst.2015.05.009 (cit. on pp. 1, 2).

[6] R. N. Kamble, P. P. Mehta, and A. Kumar. "Efavirenz self-nano-emulsifying drug delivery system: in vitro and in vivo evaluation". In: *AAPS PharmSciTech* 17 (2016), pp. 1240–1247. DOI: https://doi.org/10.1208/s12249-015-0446-2 (cit. on p. 1).

[7] S. Kaul et al. "Bioavailability in healthy adults of efavirenz capsule contents mixed with a small amount of food". In: *American Journal of Health-System Pharmacy* 67.3 (2010), pp. 217–222. DOI: https://doi.org/10.2146/ajhp090327 (cit. on p. 2).

[8] S. Kakad and S. Kshirsagar. "Nose to brain delivery of Efavirenz nanosuspension for effective neuro AIDS therapy: in-vitro, in-vivo and pharmacokinetic assessment". In: *Heliyon* 7.11 (2021). DOI: https://doi.org/10.1016/j.heliyon.2021.e08368 (cit. on pp. 2, 4).

[9] R. Jesus et al. "Synthesis and application of the MCM-41 and SBA-15 as matrices for in vitro efavirenz release study". In: *Journal of Drug Delivery Science and Technology* 31 (2016), pp. 153–159. DOI: https://doi.org/10.1016/j.jddst.2015.11.008 (cit. on pp. 2, 53).

[10] H Chavda, C Patel, and I Anand. "Biopharmaceutics classification system". In: *Systematic reviews in pharmacy* 1.1 (2010), p. 62. DOI: https://dx.doi.org/10.4103/0975-8453.59514 (cit. on p. 2).

[11] M Mehta. *Biopharmaceutics Classification System (BCS): development, implementation, and growth*. 2016 (cit. on p. 2).

[12] S. R. Vippagunta, H. G. Brittain, and D. J. Grant. "Crystalline solids". In: *Advanced drug delivery reviews* 48.1 (2001), pp. 3–26. DOI: https://doi.org/10.1016/S0169-409X(01)00097-7 (cit. on p. 2).

[13] D. Drabold. "Topics in the theory of amorphous materials". In: *The European Physical Journal B* 68 (2009), pp. 1–21. DOI: https://doi.org/10.1140/epjb/e2009-00080-0 (cit. on p. 2).

[14] W.-X. Zhou et al. "Thermal conductivity of amorphous materials". In: *Advanced Functional Materials* 30.8 (2020), p. 1903829. DOI: https://doi.org/10.1002/adfm.201903829 (cit. on p. 3).

[15] J. Aaltonen and T. Rades. "Commentary: Towards physicorelevant dissolution testing: The importance of solid-state analysis in dissolution". In: *Dissolut. Technol* 16 (2009), pp. 47–54. DOI: doi.org/10.14227/DT160209P47 (cit. on p. 3).

[16] R. Laitinen et al. "Emerging trends in the stabilization of amorphous drugs". In: *International journal of pharmaceutics* 453.1 (2013), pp. 65–79. DOI: https://doi.org/10.1016/j.ijpharm.2012.04.066 (cit. on p. 3).

[17] M. I. Ojovan and R. F. Tournier. "On structural rearrangements near the glass transition temperature in amorphous silica". In: *Materials* 14.18 (2021), p. 5235. DOI: https://doi.org/10.3390/ma14185235 (cit. on p. 3).

[18] L. Berthier and G. Biroli. "Theoretical perspective on the glass transition and amorphous materials". In: *Reviews of modern physics* 83.2 (2011), p. 587. DOI: https://doi.org/10.1103/RevModPhys.83.587 (cit. on p. 3).

[19] R. Richert. "Probing liquid dynamics, one molecule at a time". In: *Proceedings of the National Academy of Sciences* 112.16 (2015), pp. 4841–4842. DOI: https://doi.org/10.1073/pnas.1505167112 (cit. on p. 3).

[20] I. M. Kalogeras and H. E. Hagg Lobland. "The nature of the glassy state: structure and glass transitions". In: *Journal of Materials Education* 34.3 (2012), p. 69 (cit. on p. 3).

[21] P. G. Debenedetti and F. H. Stillinger. "Supercooled liquids and the glass transition". In: *Nature* 410.6825 (2001), pp. 259–267. DOI: https://doi.org/10.1038/35065704 (cit. on p. 4).

[22] C. Fandaruff et al. "Polymorphism of anti-HIV drug efavirenz: investigations on thermodynamic and dissolution properties". In: *Crystal growth & design* 14.10 (2014), pp. 4968–4975. DOI: https://doi.org/10.1021/cg500509c (cit. on pp. 4, 29).

[23] N. Y. Rakhmanina and J. N. Van den Anker. "Efavirenz in the therapy of HIV infection". In: *Expert opinion on drug metabolism & toxicology* 6.1 (2010), pp. 95–103. DOI: https://doi.org/10.1517%2F17425250903483207 (cit. on p. 4).

[24] S. M. Vrouenraets et al. "Efavirenz: a review". In: *Expert opinion on pharmacotherapy* 8.6 (2007), pp. 851–871. DOI: https://doi.org/10.1517/14656566.8.6.851 (cit. on p. 4).

[25] A. S. P. M. Arachchige and A. Arachchige. "A universal CAR-NK cell approach for HIV eradication". In: *AIMS Allergy and Immunology* 5.3 (2021), pp. 192–194. DOI: https://doi.org/10.3934/Allergy.2021015 (cit. on p. 4).

[26] a. C. Kresge et al. "Ordered mesoporous molecular sieves synthesized by a liquid-crystal template mechanism". In: *nature* 359.6397 (1992), pp. 710–712. DOI: https://doi.org/10.1038/359710a0 (cit. on p. 5).

[27] M. Manzano and M. Vallet-Regí. "Mesoporous silica nanoparticles for drug delivery". In: *Advanced functional materials* 30.2 (2020), p. 1902634. DOI: https://doi.org/10.1002/adfm.201902634 (cit. on p. 5).

[28] M Vallet-Regi et al. "A new property of MCM-41: drug delivery system". In: *Chemistry of Materials* 13.2 (2001), pp. 308–311. DOI: https://doi.org/10.1021/cm0011559 (cit. on p. 5).

[29] S Bhattacharyya, G Lelong, and M.-L. Saboungi. "Recent progress in the synthesis and selected applications of MCM-41: a short review". In: *Journal of Experimental Nanoscience* 1.3 (2006), pp. 375–395. DOI: https://doi.org/10.1080/17458080600812757 (cit. on p. 5).

[30] G. Martínez-Edo et al. "Functionalized ordered mesoporous silicas (MCM-41): Synthesis and applications in catalysis". In: *Catalysts* 8.12 (2018), p. 617. DOI: https://doi.org/10.3390/catal8120617 (cit. on p. 5).

[31] M. Vallet-Regí, F. Balas, and D. Arcos. "Mesoporous materials for drug delivery". In: *Angewandte Chemie International Edition* 46.40 (2007), pp. 7548–7558. DOI: https://doi.org/10.1002/anie.200604488 (cit. on p. 5).

[32] S. P. Hudson et al. "The biocompatibility of mesoporous silicates". In: *Biomaterials* 29.30 (2008), pp. 4045–4055. DOI: https://doi.org/10.1016/j.biomaterials.2008.07.007 (cit. on p. 6).

[33] N. A. Atiyah, T. M. Albayati, and M. A. Atiya. "Functionalization of mesoporous MCM-41 for the delivery of curcumin as an anti-inflammatory therapy". In: *Advanced Powder Technology* 33.2 (2022), p. 103417. DOI: https://doi.org/10.1016/j.apt.2021.103417 (cit. on p. 6).

[34] M. Laghaei et al. "The effect of various types of post-synthetic modifications on the structure and properties of MCM-41 mesoporous silica". In: *Progress in Organic Coatings* 90 (2016), pp. 163–170. DOI: https://doi.org/10.1016/j.porgcoat.2015.10.007 (cit. on p. 6).

[35] A. Datt, I. El-Maazawi, and S. C. Larsen. "Aspirin loading and release from MCM-41 functionalized with aminopropyl groups via co-condensation or postsynthesis modification methods". In: *The Journal of Physical Chemistry C* 116.34 (2012), pp. 18358–18366. DOI: https://doi.org/10.1021/jp3063959 (cit. on p. 6).

[36] C. Berthomieu and R. Hienerwadel. "Fourier transform infrared (FTIR) spectroscopy". In: *Photosynthesis research* 101 (2009), pp. 157–170. DOI: https://doi.org/10.1007/s11120-009-9439-x (cit. on p. 6).

[37] W. Perkins. "Fourier transform-infrared spectroscopy: Part l. Instrumentation". In: *Journal of Chemical Education* 63.1 (1986), A5. DOI: https://doi.org/10.1021/ed063pA5 (cit. on p. 7).

[38] M.-M. Blum and H. John. "Historical perspective and modern applications of attenuated total reflectance–Fourier transform infrared spectroscopy (ATR-FTIR)". In: *Drug testing and analysis* 4.3-4 (2012), pp. 298–302. DOI: https://doi.org/10.1002/dta.374 (cit. on p. 7).

[39] C. S. Kumar. *Transmission electron microscopy characterization of nanomaterials*. Springer Science & Business Media, 2013. DOI: https://doi.org/10.1007/978-3-642-38934-4 (cit. on p. 7).

[40] B. J. Inkson. "Scanning electron microscopy (SEM) and transmission electron microscopy (TEM) for materials characterization". In: *Materials characterization using nondestructive evaluation (NDE) methods*. Elsevier, 2016, pp. 17–43. DOI: https://doi.org/10.1016/B978-0-08-100040-3.00002-X (cit. on p. 7).

[41] K. Lukas and P. K. LeMair. "Differential Scanning Calorimetry: Fundamental Overview." In: *Resonance: Journal of Science Education* 14.8 (2009). DOI: https://doi.org/10.1007/s12045-009-0076-7 (cit. on p. 8).

[42] S.-D. Clas, C. R. Dalton, and B. C. Hancock. "Differential scanning calorimetry: applications in drug development". In: *Pharmaceutical science & technology today* 2.8 (1999), pp. 311–320. DOI: https://doi.org/10.1016/s1461-5347(99)00181-9 (cit. on pp. 9, 10).

[43] G. Smith et al. "Dielectric relaxation spectroscopy and some applications in the pharmaceutical sciences". In: *Journal of pharmaceutical sciences* 84.9 (1995), pp. 1029–1044. DOI: https://doi.org/10.1002/jps.2600840902 (cit. on pp. 10, 11).

[44] F. Kremer and A. Schönhals. *Broadband dielectric spectroscopy*. Springer Science & Business Media, 2002 (cit. on p. 10).

[45] J. B. Lambert, E. P. Mazzola, and C. D. Ridge. *Nuclear magnetic resonance spectroscopy: an introduction to principles, applications, and experimental methods*. John Wiley & Sons, 2019 (cit. on p. 11).

[46] Q. Li and C. Kang. "A practical perspective on the roles of solution NMR spectroscopy in drug discovery". In: *Molecules* 25.13 (2020), p. 2974. DOI: https://doi.org/10.3390%2Fmolecules25132974 (cit. on p. 11).

[47] C. I. Crucho, C. Baleiza o, and J. P. S. Farinha. "Functional group coverage and conversion quantification in nanostructured silica by 1H NMR". In: *Analytical chemistry* 89.1 (2017), pp. 681–687. DOI: https://doi.org/10.1021/acs.analchem.6b03117 (cit. on pp. 11, 25).

[48] M. Picollo, M. Aceto, and T. Vitorino. "UV-Vis spectroscopy". In: *Physical sciences reviews* 4.4 (2018), p. 20180008. DOI: 10.1515/psr-2018-0008 (cit. on p. 11).

[49] G. Verma and M. Mishra. "Development and optimization of UV-Vis spectroscopy-a review". In: *World J. Pharm. Res* 7.11 (2018), pp. 1170–1180. DOI: 10.20959/wjpr201811-12333 (cit. on p. 11).

[50] M. Grün et al. "Novel pathways for the preparation of mesoporous MCM-41 materials: control of porosity and morphology". In: *Microporous and mesoporous materials* 27.2-3 (1999), pp. 207–216. DOI: https://doi.org/10.1016/S1387-1811(98)00255-8 (cit. on p. 13).

[51] P. Iliade et al. "Functionalization of mesoporous MCM-41 with aminopropyl groups by co-condensation and grafting: a physico-chemical characterization". In: *Research on Chemical Intermediates* 38 (2012), pp. 785–794. DOI: https://doi.org/10.1007/s11164-011-0417-5 (cit. on p. 13).

[52] M. Thommes et al. "Physisorption of gases, with special reference to the evaluation of surface area and pore size distribution (IUPAC Technical Report)". In: *Pure and applied chemistry* 87.9-10 (2015), pp. 1051–1069. DOI: https://doi.org/10.1515/pac-2014-1117 (cit. on p. 17).

[53] J. A. S. Costa et al. "Efficient adsorption of a mixture of polycyclic aromatic hydrocarbons (PAHs) by Si–MCM–41 mesoporous molecular sieve". In: *Powder Technology* 308 (2017), pp. 434–441. DOI: https://doi.org/10.1016/j.powtec.2016.12.035 (cit. on p. 18).

[54] M Manzano et al. "Studies on MCM-41 mesoporous silica for drug delivery: effect of particle morphology and amine functionalization". In: *Chemical Engineering Journal* 137.1 (2008), pp. 30–37. DOI: https://doi.org/10.1016/j.cej.2007.07.078 (cit. on p. 18).

[55] J. Coates. *Interpretation of infrared spectra, a practical approach*. 2000. DOI: https://doi.org/10.1002/9780470027318.a5606 (cit. on p. 18).

[56] S. K. Parida et al. "Adsorption of organic molecules on silica surface". In: *Advances in colloid and interface science* 121.1-3 (2006), pp. 77–110. DOI: https://doi.org/10.1016/j.cis.2006.05.028 (cit. on p. 19).

[57] N. P. Reddy et al. "FTIR spectroscopy for estimation of efavirenz in raw material and tablet dosage form". In: *International Current Pharmaceutical Journal* 4.6 (2015), pp. 390–395 (cit. on p. 22).

[58] B. Baumgartner et al. "Pore size-dependent structure of confined water in mesoporous silica films from water adsorption/desorption using ATR–FTIR spectroscopy". In: *Langmuir* 35.37 (2019), pp. 11986–11994. DOI: https://doi.org/10.1021/acs.langmuir.9b01435 (cit. on p. 23).

[59] S. Sathigari et al. "Physicochemical characterization of efavirenz–cyclodextrin inclusion complexes". In: *Aaps Pharmscitech* 10.1 (2009), pp. 81–87. DOI: https://doi.org/10.1208%2Fs12249-008-9180-3 (cit. on p. 29).

[60] J. J. M. Ramos et al. "Thermal behavior and slow relaxation dynamics in amorphous efavirenz: A study by DSC, XRPD, TSDC, and DRS". In: *Journal of Pharmaceutical Sciences* 108.3 (2019), pp. 1254–1263. DOI: https://doi.org/10.1016/j.xphs.2018.10.050 (cit. on pp. 29, 52).

[61] R. Underwood, J. Tomlinson-Phillips, and D. Ben-Amotz. "Are long-chain alkanes hydrophilic?" In: *The Journal of Physical Chemistry B* 114.26 (2010), pp. 8646–8651. DOI: https://doi.org/10.1021/jp912089q (cit. on p. 37).

[62] T. Cordeiro et al. "Accessing the physical state and molecular mobility of naproxen confined to nanoporous silica matrixes". In: *The Journal of Physical Chemistry C* 120.26 (2016), pp. 14390–14401. DOI: https://doi.org/10.1021/acs.jpcc.6b04078 (cit. on p. 38).

[63] S Havriliak and S Negami. "A complex plane analysis of α-dispersions in some polymer systems". In: *Journal of Polymer Science Part C: Polymer Symposia*. Vol. 14. 1. Wiley Online Library. 1966, pp. 99–117. DOI: https://doi.org/10.1002/polc.5070140111 (cit. on p. 41).

[64] M. Viciosa and M Dionısio. "Molecular mobility and fragility in n-ethylene glycol dimethacrylate monomers". In: *Journal of non-crystalline solids* 341.1-3 (2004), pp. 60–67. DOI: https://doi.org/10.1016/j.jnoncrysol.2004.04.018 (cit. on pp. 42, 52).

[65] A. B. Unni et al. "Vapor-Deposited Thin Films: Studying Crystallization and α-relaxation Dynamics of the Molecular Drug Celecoxib". In: *The Journal of Physical Chemistry B* 126.20 (2022), pp. 3789–3798. DOI: https://doi.org/10.1021/acs.jpcb.2c01284 (cit. on p. 42).

[66] S. Baghel et al. "An investigation into the crystallization tendency/kinetics of amorphous active pharmaceutical ingredients: A case study with dipyridamole and cinnarizine". In: *European Journal of Pharmaceutics and Biopharmaceutics* 104 (2016), pp. 59–71. DOI: https://doi.org/10.1016/j.ejpb.2016.04.017 (cit. on p. 43).

[67] A. Brás et al. "Molecular mobility of nematic E7 confined to molecular sieves with a low filling degree". In: *The Journal of chemical physics* 132.22 (2010). DOI: https://doi.org/10.1063/1.3432775 (cit. on p. 45).

[68] A. Schönhals and F Kremer. "Analysis of dielectric spectra". In: *Broadband dielectric spectroscopy*. Springer, 2003, pp. 59–98. DOI: https://doi.org/10.1007/978-3-642-56120-7_3 (cit. on p. 45).

[69] S. Inocencio et al. "Ibuprofen incorporated into unmodified and modified mesoporous silica: From matrix synthesis to drug release". In: *Microporous and Mesoporous Materials* 310 (2021), p. 110541. DOI: https://doi.org/10.1016/j.micromeso.2020.110541 (cit. on pp. 46, 47).

[70] G. Figari et al. "Understanding Fenofibrate Release from Bare and Modified Mesoporous Silica Nanoparticles". In: *Pharmaceutics* 15.6 (2023), p. 1624. DOI: https://doi.org/10.3390/pharmaceutics15061624 (cit. on pp. 46, 47).

[71] I. Popov et al. "The mechanism of the dielectric relaxation in water". In: *Physical Chemistry Chemical Physics* 18.20 (2016), pp. 13941–13953. DOI: https://doi.org/10.1039/C6CP02195F (cit. on p. 47).

[72] G. Wilson et al. "Dielectric properties of ices II, III, V, and VI". In: *The journal of chemical physics* 43.7 (1965), pp. 2384–2391. DOI: https://doi.org/10.1063/1.1697137 (cit. on p. 47).

[73] L Frunza et al. "Relaxation processes of water confined to AlMCM-41 molecular sieves. Influence of the hydroxyl groups of the pore surface". In: *The European Physical Journal E* 26 (2008), pp. 379–386. DOI: https://doi.org/10.1140/epje/i2007-10340-y (cit. on p. 48).

[74] C. Angell. "Relaxation in liquids, polymers and plastic crystals—strong/fragile patterns and problems". In: *Journal of Non-Crystalline Solids* 131 (1991), pp. 13–31. DOI: https://doi.org/10.1016/0022-3093(91)90266-9 (cit. on p. 51).

[75] Q. Gao and Z. Jian. "Measured and ideal glass transition temperatures of glass-forming liquids". In: *Journal of Molecular Liquids* 296 (2019), p. 111962. DOI: https://doi.org/10.1016/j.molliq.2019.111962 (cit. on p. 51).

[76] A. R. Brás et al. "Molecular motions in amorphous ibuprofen as studied by broadband dielectric spectroscopy". In: *The Journal of Physical Chemistry B* 112.35 (2008), pp. 11087–11099. DOI: https://doi.org/10.1021/jp8040428 (cit. on p. 51).

[77] I. Avramov. "Viscosity in disordered media". In: *Journal of non-crystalline solids* 351.40-42 (2005), pp. 3163–3173. DOI: https://doi.org/10.1016/j.jnoncrysol.2005.08.021 (cit. on p. 52).

[78] C. Racles et al. "Functionalized Mesoporous Silica as Doxorubicin Carriers and Cytotoxicity Boosters". In: *Nanomaterials* 12.11 (2022), p. 1823. DOI: https://doi.org/10.3390/nano12111823 (cit. on p. 54).

[79] M. H. Mashhadizadeh and M. Amoli-Diva. "Drug-carrying amino silane coated magnetic nanoparticles as potential vehicles for delivery of antibiotics". In: *J. Nanomed. Nanotechnol* 3.4 (2012), p. 1. DOI: http://dx.doi.org/10.4172/2157-7439.1000139 (cit. on p. 54).

[80] P. P. Santos. "Reações Ácido-Base". In: *Química Orgânica*. Ed. by I. PressEditor. 2nd. Vol. 1. IST - Instituto Superior Técnico, 2012, 200–201 (cit. on p. 54).

[81] M. J. O'Neil (cit. on p. 54).

A

Appendices

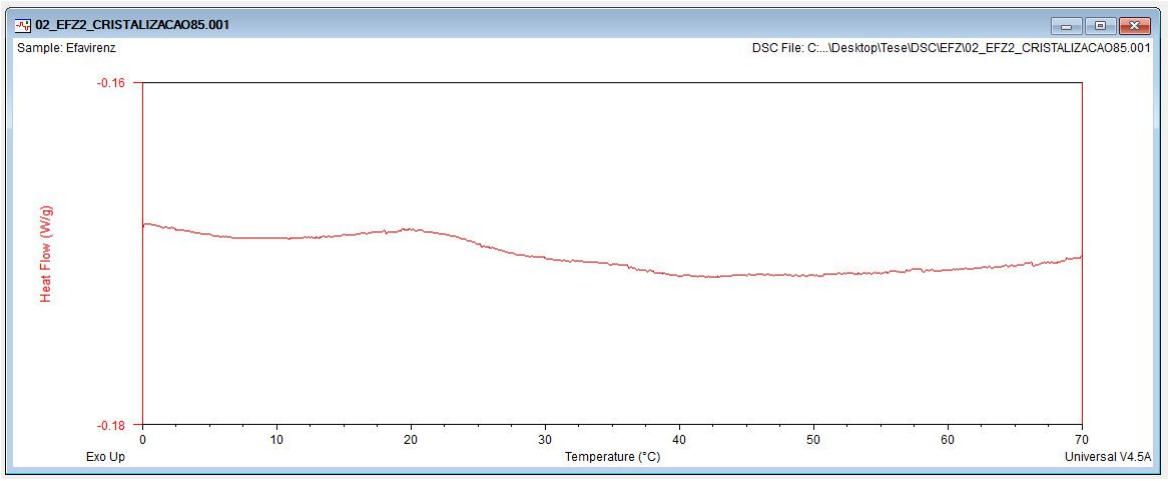

Figure A.1: Thermogram obtained on heating at 10 °C/min after isothermal crystallization at 85 °C, for the 0-70 °C.

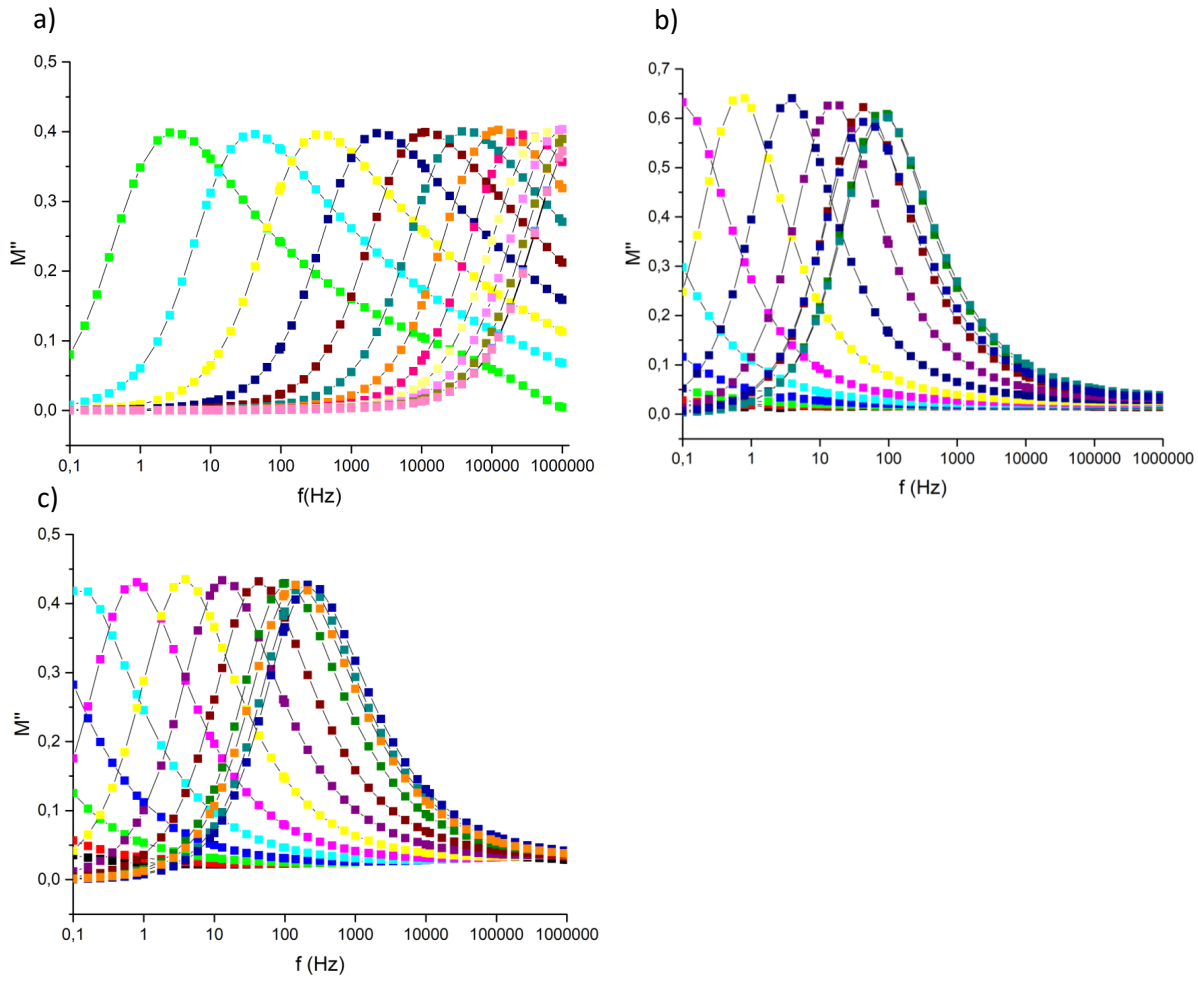

Figure A.2: Isothermal M" spectra of: a) NH_2-MCM-41, b)CH_3-MCM-41 and c)SH-MCM-41 for temperatures from -100 to 10 °C every 10 degrees.

2023 MODIFYING THE SURFACE OF MESOPOROUS SILICA FOR TUNING THE DRUG RELEASE PROFILE Daniela Leonardo Duarte

NOVA SCHOOL OF SCIENCE & TECHNOLOGY